

2012

A Device for Measuring Thermal Conductivity of Molten Salt Nitrates at Elevated Temperatures for Use in Solar Thermal Power Applications

Spencer Nelle
Lehigh University

Follow this and additional works at: <http://preserve.lehigh.edu/etd>

Recommended Citation

Nelle, Spencer, "A Device for Measuring Thermal Conductivity of Molten Salt Nitrates at Elevated Temperatures for Use in Solar Thermal Power Applications" (2012). *Theses and Dissertations*. Paper 1079.

This Thesis is brought to you for free and open access by Lehigh Preserve. It has been accepted for inclusion in Theses and Dissertations by an authorized administrator of Lehigh Preserve. For more information, please contact preserve@lehigh.edu.

A Device for Measuring Thermal Conductivity of Molten Salt Nitrates at Elevated
Temperatures for Use in Solar Thermal Power Applications

By

Spencer J. Nelle

A Thesis

Presented to the Graduate and Research Committee

of Lehigh University

in Candidacy for the Degree of

Master of Science

in

Mechanical Engineering and Mechanics

Lehigh University

May 2012

© 2012
Spencer J. Nelle
All Rights Reserved

This thesis is accepted and approved in partial fulfillment of the requirements for the
Master of Science in Mechanical Engineering

Characterization of Thermo-Physical Properties of Molten Salt Nitrates for Use in Solar
Thermal Power Applications
Spencer J. Nelle

Date Approved

Dr. Alp Oztekin
Advisor

Dr. Sudhakar Neti
Co-Advisor

Dr. Gary Harlow
Department Chair Person

Acknowledgements

The author would like to thank all those who contributed to the research presented in this thesis. Thank you to Dr. Alp Oztekin for his guidance while developing heat transfer simulations, designing the thermal conductivity test rig, and calibrating the apparatus. Thank you to Dr. Sudhakar Neti for lending his expertise in designing the test rig and the accompanying experimental setup. The author would also like to thank Dr.'s Oztekin and Neti for their time devoted as mentors and for their contributions towards the author's professional development.

Thank you to Dr. Satish Mohapatra for his help developing the thermal conductivity test rig and for providing expertise related to chemical engineering concerns this project faced. Thank you to Dynalene, Inc. for repeated use of its facilities and instruments. Thank you to Dr. Ray Pearson for providing the author with equipment and lab resources for viscosity data collection. Thank you to Bill Maroun for his help fabricating the test rig. Thank you to Tim Nixon for his expertise in selecting vital sensor equipment and helping with device calibration and electronics setup. Thank you to Kevin Coscia for conducting accompanying research vital to the design of the thermal conductivity device. Thank you to Tucker Elliot for providing valuable input into the design of the thermal conductivity device and for his programming expertise. Thank you to Benjamin Rosenzweig for his help in developing a calibration procedure for the thermal conductivity instrument.

Lastly, I would like to thank my family for their love and support.

TABLE OF CONTENTS

	Page
ACKNOWLEDGEMENTS	IV
LIST OF TABLES	VI
LIST OF FIGURES	VII
LIST OF NOMENCLATURE	X
ABSTRACT	1
1: INTRODUCTION	2
2: LITERATURE REVIEW	6
3: INSTRUMENTATION/EXPERIMENTAL SETUP	10
4: DESIGN AND FABRICATION	16
5: THERMAL ANALYSIS	22
5.1: PRESSURE DROP AND HEAT LOSS SIMULATION OF CSP NIGHT OPERATION	22
5.2: THERMAL CONDUCTIVITY CELL FINITE ELEMENT SIMULATIONS	29
6: CALIBRATION	35
6.1: ANALYTICAL SOLUTION FOR THIN LINE HEAT SOURCE	35
6.2: RESISTANCE AND TEMPERATURE CALIBRATION	37
7: RESULTS AND DISCUSSION	39
7.1: VISCOSITY	39
7.2: THERMAL CONDUCTIVITY	44
8: CONCLUSIONS	50
9: FUTURE WORK	52
REFERENCES	53
VITA	55

LIST OF TABLES

Table 1: Rheometer operation procedure for molten salt viscosity data collection.....	11
Table 2: Shear Thinning test procedure for molten salt viscosity data collection.	13
Table 3: Thermal Conductivity test procedure for molten salt data collection.....	14
Table 4: Major design parameters for thermal conductivity cell.	16
Table 5: Activation energies calculated for each molten salt using the Arrhenius model for liquid viscosities as a function of temperature compared to literature values.	43

LIST OF FIGURES

Figure 1: ARES Rheometer mounted with couette fixture and open furnace door.	10
Figure 2: ARES Couette Fixture components. Spindle (left) and Cup (right).....	10
Figure 3: A) Couette Fixture mounted with open furnace door. B) Detail view of proper meniscus prior to testing.	12
Figure 4: Schematic detailing proper meniscus position in relation to cup.....	12
Figure 5: Schematic showing temperature profile of wire heating, plotting Temperature (°C) vs. Time (s).	16
Figure 6: 2D CAD drawing (side view) of platinum wire and stainless steel bracket arm.	18
Figure 7: 2D CAD drawing of device circuit and base, A) transparent, and B) assembled.	18
Figure 8: Close up view of L-shaped bracket.	19
Figure 9: Close-up view of mechanical and electrical contacts between cap, bracket, and wire.	20
Figure 10: 3D CAD drawing of thermal conductivity device.....	21
Figure 11: Solar receiver cross section.	22
Figure 12: Pumping Power (W/m) vs. Temperature (°C) for LiNaK-NO ₃	27
Figure 13: Heat Loss (W/m) vs. Temperature (°C) for LiNaK-NO ₃	27
Figure 14: A) Coarse B) Medium and C) Fine Mesh Geometries used in Transient Thermal analysis using ANSYS	31

Figure 15: Temperature ($^{\circ}\text{C}$) vs. Time (s) for 1 mm Platinum Wire. Three different mesh sizes were tested and plotted: coarse, medium, and fine.	32
Figure 16: Temperature ($^{\circ}\text{C}$) vs. Time (s) for 1 mm Platinum Wire. Four different time step sizes were tested and plotted: 0.005, 0.01, 0.1, and 0.5.	33
Figure 17: Resistance (Ω) vs. Temperature ($^{\circ}\text{C}$) for 1mm Platinum Wire thermal conductivity device immersed in distilled H_2O	37
Figure 18: Temperature ($^{\circ}\text{C}$) vs. Time (s) comparison of theoretical simulation and experimental data.	38
Figure 19: Viscosity (P) vs. Shear Rate (1/s) for LiNaK-NO_3 tested at 5 different temperatures, 160°C , 250°C , 300°C , 350°C , and 450°C	39
Figure 20: Viscosity (cP) vs. Temperature ($^{\circ}\text{C}$) from melting temperature up to 550°C for four different molten salts, LiNaK-NO_3 , NaK-NO_3 , LiNa-NO_3 , and LiK-NO_3	41
Figure 21: Viscosity (cP) vs. Temperature ($^{\circ}\text{C}$) from melting temperature up to 550°C for A) LiNaK-NO_3 and B) NaK-NO_3 plotted with Arrhenius Fit line.	42
Figure 22: Viscosity (cP) vs. Temperature ($^{\circ}\text{C}$) from melting temperature up to 550°C for A) LiNa-NO_3 and B) LiK-NO_3 plotted with Arrhenius Fit line.	42
Figure 23: Resistance (Ω) vs. Time (s) for 1 mm diameter platinum wire under 3 Amps of current, immersed in 22°C distilled H_2O	44
Figure 24: Temperature ($^{\circ}\text{C}$) vs. Time (s) measured with 3 Amps of current applied to 1 mm platinum wire for 5 seconds immersed in distilled H_2O at 22°C and simulated with ANSYS.	45
Figure 25: λ (W/m K) vs. Temperature ($^{\circ}\text{C}$) for distilled H_2O near 23°C	46

Figure 26: Resistance (Ω) vs. Time (s) for 1 mm diameter platinum wire under 3 Amps of current, immersed in 24°C Propylene Glycol. 47

Figure 27: Temperature ($^{\circ}\text{C}$) vs. Time (s) measured with 3 Amps of current applied to 1 mm platinum wire for 5 seconds immersed in Propylene Glycol at 24°C. 47

Figure 28: λ (W/m K) vs. Temperature ($^{\circ}\text{C}$) for Propylene Glycol from 24-100°C. 48

LIST OF NOMENCLATURE

ΔT	Temperature change ($^{\circ}\text{C}$)
q	Heat generated via joule heating per unit volume (W/m^3),
r	Radial distance in (m), or radius (m)
C	Euler's constant
α	Thermal diffusivity (m^2/s)
t	Time (s)
$\lambda(T,P)$	Thermal conductivity as a function of the temperature pressure of a fluid.
τ	Shear stress (Pa)
$\frac{\partial u}{\partial x}$	The change in velocity across the thickness of a fluid
μ	Viscosity of a fluid.
S	Slope of the linear portion of the ΔT vs. $\ln(t)$ curve
$T_{g,o}$	The temperature of the outside of the glass envelope
$T_{g,i}$	The temperature of the inside of the glass envelope
$T_{s,o}$	The temperature of the outside of the solar receiver
$T_{s,i}$	The temperature of the inside of the solar receiver
$r_{s,i}$	The inner radius of the solar receiver which is 0.070 m
$t_{s,o}$	The thickness of the solar receiver wall which is 0.002 m
t_g	The thickness of the glass envelope, which is 0.001 m
T_{∞}	The ambient temperature outside the envelope is 15°C
T_f	The temperature of the fluid, which varies between 150 and 550°C
h_{forced}	The convection coefficient associated with the flow of fluid pumped through the inner radius of the pipe in (W/m^2)
k_s	The thermal conductivity of the steel pipe ($\text{W}/\text{m K}$)
ϵ_g	The emissivity of the glass envelope
ϵ_s	The emissivity of the steel pipe
σ	The Stefan-Boltzmann constant defined as 5.670373×10^{-8} ($\text{W m}^{-2} \text{K}^{-4}$)
h_{free}	The convection coefficient of free convection due to air interface on the glass envelope outer surface (W/m^2)
Nu_D	The ratio of convective to conductive heat transfer normal to the diameter of the steel pipe
Re_D	The ratio of inertial forces to viscous forces occurring in the steel pipe
Pr	The ratio of kinematic viscosity to thermal diffusivity
f	Darcy friction factor, represents friction losses in closed pipe flow
ΔP	The pressure drop in the pipe (Pa)
ρ_{fluid}	The density of the fluid inside the pipe
L	The length of the pipe (m)
v_{fluid}	The fluid velocity (m/s)
Ra	The relationship between density forces and viscous forces in ambient air
Nu	Nusselt Number for free convection; the ratio of convective to conductive heat transfer normal to the diameter of the outer glass envelope
θ_n	Dimensionless temperature ratio between 0 and 1
μ_0	The viscosity of the fluid at a reference temperature

b	A coefficient governing the rate of decrease of viscosity with temperature
E	The activation energy of the fluid
R	The universal gas constant.
ν_{fluid}	The kinematic viscosity of the fluid (m^2/s)
α_{fluid}	The thermal diffusivity of the fluid (m^2/s)
μ_{fluid}	The viscosity of the fluid (Poise)
g	Acceleration due to Earth's gravity (m^2/s)
β	Thermal expansion coefficient by volume ($1/^\circ C$)
$\frac{\partial T}{\partial n}$	Change in temperature with respect to any axial ordinate, x, y, or z.
ρ_w	Density of platinum wire (kg/m^3)
k_w	Thermal conductivity of platinum wire (W/m K)
$C_{p,w}$	Specific heat of platinum wire (J/kg C)
$C_{p,fluid}$	Specific heat of test fluid (J/ kg C)
k_{fluid}	Thermal conductivity of test fluid (W/ mK)
ν_{air}	The kinematic viscosity of ambient air (m^2/s)
α_{air}	The thermal diffusivity of ambient air (m^2/s)

Abstract

Binary and Ternary mixtures of Molten Salt Nitrates are ideal candidates for future concentrating solar power (CSP) plant heat transfer fluids (HTFs) because of their high operating temperature limits resulting in greater Rankine efficiency. The inclusion of these HTFs into CSP plants is expected to revolutionize the industry by allowing for energy and cost savings that are attractive to potential plant developers and investors. It is vital for plant designers to have access to fully characterized thermo-physical properties of the intended HTFs, with thermal conductivity, viscosity, and specific heat capacity being the most crucial. Existing literature has not fully elucidated the thermo-physical properties of binary and ternary molten salt nitrates through their operating temperature range. This work presents the viscosity of eutectic ternary and binary compositions of molten alkali salt nitrates (Li-NO_3 , K-NO_3 , and Na-NO_3) up to 550°C . A device to measure the thermal conductivity of these salts with accuracy at elevated temperatures was designed and built as no commercial offerings are able to withstand the corrosive nature of molten salt at high temperatures. The device is shown to accurately measure the thermal conductivity of water at room temperature. The present work is a step towards fully characterizing the thermo-physical properties of the aforementioned molten salts.

1: Introduction

Viscosity and thermal conductivity are two vital thermo-physical properties for the design of CSP systems. Currently, there are two types of systems in practice used to capture energy from the Sun's rays and transfer it to electric power for consumer use.

The first type, known as parabolic troughs, consist of an array of long, curved reflectors which focus inbound light onto a cylindrical receiver (pipe, or tube) containing heat transfer fluid. Heat is first transferred from solar radiation onto the wall of the receiver. Thermal energy then conducts through the pipe wall until it meets the moving heat transfer fluid, where it can transfer via both conduction and convection. The raised temperature of the outer surface of the receiver (due to the incident, focused solar radiation) creates a temperature gradient within the pipe wall, as the fluid/wall interface is initially at a lower temperature. This temperature gradient is the driver for conduction of thermal energy to occur through the receiver wall. Thermal energy is further transferred into the circulating heat transfer fluid through convection. Piping runs throughout the array and carries the heat transfer fluid to the steam generator.

The second type, known as solar power towers, consist of an array of movable mirrors surrounding a central tower containing a large tank which holds a significant volume of heat transfer fluid at its top. Each heliostat is positioned to reflect solar radiation onto the tower. Similar to the aforementioned parabolic trough method, the intensity of the solar radiation incident on the tank's container walls creates a temperature gradient driving conduction of thermal energy through the wall into the bulk heat transfer fluid via conduction and convection. Piping runs from the bottom to

the top of the tower in order to circulate the hot heat transfer fluid to the steam generator.

The thermal energy within the heat transfer fluid is used to heat water past its vaporization temperature in order to influence a phase change to steam which is used to drive a steam turbine and produce electricity.

The thermodynamic efficiency of this cycle can be improved through several methods. Ideally, the temperature of the heat transfer fluid is as high as possible during steam generation as it produces a higher quality steam on a unit mass basis, capable of doing more work on the turbine, and resulting in greater electricity generation.

Increasing the ability of the heat transfer fluid to store more heat per unit mass (known as specific heat capacity) allows more potential energy to convert to work at the site of steam generation. Reducing the power required to circulate the heat transfer fluid throughout the plant will also increase the cycle's efficiency. This can be achieved by selecting a heat transfer fluid with as low a viscosity as possible within the plant operating range. For the purposes of this work, the operating range was approximated to be between 100-600°C, as the actual range will vary depending on plant design features. At the steam generator, which acts as a heat exchanger between the heat transfer fluid and liquid water to be converted to steam, the heat transfer rate can be increased by selecting a heat transfer fluid with a maximum heat transfer coefficient, assuming the surface area and temperature gradient between HTF and surface are constant. The thermal conductivity of the fluid is an important underlying thermo-physical property to the derived heat transfer coefficient. In order to optimize the physical dimensions of

each of the plant features, such as the steam generator, pipe wall thickness, etc., engineers require a thorough understanding of the thermo-physical properties of the heat transfer fluid: namely viscosity and thermal conductivity.

Molten Alkali-Nitrate salts are a particularly interesting candidate for further concentrated solar power development due to several of their material thermal and physical properties. These salts in their liquid state, referred to as molten due to the high temperatures involved, are workable in the sense their viscosities are believed to be relatively low at high temperature allowing them to be pumped without excessively large power input. For example, Alkali-Nitrate salts such as NaNO_3 exist as solids up to 308°C , and do not thermally degrade until a temperature of $\sim 600^\circ\text{C}$ is reached. Compared to the current heat transfer fluid used in parabolic trough concentrated solar power plants, silicon based oils, Alkali-Nitrate molten salts have higher specific heat capacity (measured in J/g K). The thermal conductivity of Alkali-Nitrate salts are believed to be akin to water throughout their operating temperature range. While NaNO_3 , KNO_3 , and LiNO_3 are of primary interest because of the aforementioned properties which offer improved heat transfer characteristics compared to silicon based oils, the high melting temperatures means excessively large amounts of heat would be required to be input to the salt at all times to maintain it in a liquid state. Consequently, binary and tertiary eutectic mixtures of these salts have been proposed to lower the melting point of the heat transfer fluid, widening the operating temperature range and reducing the amount of heat required to keep the salt in its molten form. The binary eutectic molten salts studied in this work are 50:50 Sodium-Potassium Nitrate (NaK-

NO_3), 56:44 Lithium-Sodium Nitrate (LiNa-NO_3), and 43:57 Lithium-Potassium Nitrate (LiK-NO_3). The ternary eutectic molten salt mixture studied in this work is 30:21:49 Lithium-Sodium-Potassium Nitrate (LiNaK-NO_3).

The viscosity of the heat transfer fluid is measured using a concentric cylinder rheometer. While viscometers are another potential candidate to produce this data, the rheometer outfitted with a high temperature furnace allows shear-thinning characteristics of the fluid to be analyzed. Additionally, the rheometer allows viscosity to be measured as a function of operating temperature.

The thermal conductivity of the heat transfer fluid can be measured using the transient hot wire method. By applying a pulse of current to a long, thin platinum wire submerged in the heat transfer fluid, a process known as Joule heating enacts a temperature rise in the wire. A temperature gradient is formed across the outer surface of the platinum wire and the stationary heat transfer fluid (to rule out convection contributing to the heat transfer). As a result of the temperature increase, the resistance of the wire changes inducing a change in voltage read by the sensing equipment. This voltage change is recorded as a function of time and is used to calculate the thermal conductivity of the salt via a calibration to a heat transfer model of the system.

The following sections are organized into Literature Review, encompassing current and past research relevant to the present work, Instrumentation/Experimental Setup, Design and Fabrication, Thermal Analysis, Calibration, Results and Discussion, Conclusions, and Future Work.

2: Literature Review

Important properties of Molten Alkali-Nitrate salts have not been fully characterized. For example, while the melting points of each single component salt are well known with NaNO_3 at 306°C^1 , KNO_3 at 333°C^2 , LiNO_3 at 255°C^3 , only a set of incomplete data is available for density, specific heat, thermal conductivity and viscosity as a function of temperature. These properties are publicly available for single component salts in their solid states (i.e. below their melting temperatures), but data above this threshold is both scarce and of primary importance to further the development of concentrated solar power applications. Furthermore, the above properties for LiK-NO_3 , LiNa-NO_3 , NaK-NO_3 , and LiNaK-NO_3 have not been fully elucidated over the intended molten operating temperature ranges.

Data for the specific heat capacity of these molten salts is available for the binary mixtures at select temperatures. Literature revealed a specific heat of 1.502 J/g K for the eutectic composition of NaK-NO_3 at 497°C^4 . Data for the specific heat capacity of the ternary eutectic (LiNaK-NO_3) salt was not found. There is limited published data over the entire molten temperature range of the salts of interest.

Viscosity data has been revealed for single component molten alkali nitrate salts covering a portion of the intended operating temperature range. Molten NaNO_3 at 480°C was found to have a viscosity of $1.43 \text{ centiPoise (cP)}^5$. Similar results were found for KNO_3^6 and LiNO_3^7 . Viscosities of closely related binary and ternary molten salt mixtures were published up to 200°C by researchers at Sandia National Laboratories, but the data can serve only as a guide for the present work given the compounds are

slightly different and were not studied over the entire operating range⁷. Beyond searching for viscosity data as a function of temperature, shear-thinning data was sought after for the molten alkali-nitrate salts, and no relevant research was found.

Thermal conductivity data for the compounds of interest suffered from the same problems as viscosity data. Incomplete data sets representing thermal conductivity data over the lower end of the operating temperature range are available, but many gaps exist in this knowledge base. Even then, the limited data available is not widely agreed upon across many authors due to the difficulty in applying current thermal conductivity detection methods to molten alkali-nitrate salts. Due to the corrosive nature of these molten salts at elevated temperatures, many existing thermal conductivity apparatuses are inappropriate for detection. As an example, NaNO₃ was shown by Nagashima and Nagasaki⁸ to have a thermal conductivity of 0.500 W/m K at 397°C, while Gustafsson et al.⁹ and McLaughlin et al.¹⁰ found a thermal conductivity for NaNO₃ of 0.550 W/m K at the same temperature.

A literature search was conducted to make an informed decision regarding the best possible testing method to use in order to detect the thermal conductivity of the molten alkali-nitrate salts. According to research presented by Nagashima and Nagasaki⁸, steady state methods are sources of significant error due to their inability to rule out the contribution of convection to the overall heat transfer to the system. Therefore, transient methods utilizing a short pulse of heat input to the sample are ideal. Several prominent transient methods were considered and ultimately ruled out: concentric cylinder¹¹, vacuum cylinder¹², and plane source¹³. The transient hot wire

method¹⁴ offered the optimal combination of design simplicity, accurate measurements, and small size. The transient hot wire method uses a short metallic wire (typically platinum) in contact with the sample fluid. A short, large current is passed through the wire to produce a small (typically no more than 5°C) temperature rise in the wire, which conducts heat into the sample fluid. As the temperature of the wire decreases after the pulse is shut off, the resistance of the platinum wire changes slightly effecting a voltage change¹⁵. The voltage of the entire circuit is analyzed as a function of time by a data acquisition system. Using analytical relations for a thin line heat source^{15,16,17} in an infinite medium, the thermal conductivity can be calculated. The fundamental working equation for the transient hot wire technique is presented below¹⁵:

$$\Delta T = \frac{q}{4\pi\lambda(T, P)} \ln \frac{4\alpha t}{r^2 C} \quad (2.1)$$

where ΔT represents the temperature change in the wire (°C), q represents the heat generated via joule heating per unit volume in the wire (W/m³), r represents the radius of the platinum wire, C represents Euler's constant, α represents the thermal diffusivity of the fluid (m²/s), t represents time in seconds, and $\lambda(T, P)$ represents the thermal conductivity of the fluid, noting it is a function of the temperature as well as the pressure of the fluid.

Details regarding the design, construction, and calibration of the transient hot wire device are contained in the present work. Electrical design parameters were reviewed as well to determine the instrumentation required to detect the anticipated

signal voltages. At the operating temperatures of the device (up to 600°C), drive voltages of 100 mV have been used in similarly designed devices¹⁶.

3: Instrumentation/Experimental Setup

An ARES rheometer using a couette fixture was used in conjunction with TA Instruments graphical interface software to sample and collect viscosity data as a function of temperature and shear rate.



Figure 1: ARES Rheometer mounted with couette fixture and open furnace door.

The cup piece has the dimensions: 27 mm inner diameter, 38 mm height, 21,760 mm³ volume. The spindle portion has the dimensions: 25 mm outer diameter, 32 mm height, and 15,700 mm³ volume. A typical sample was approximately 6000 mm³ of molten salt.



Figure 2: ARES Couette Fixture components. Spindle (left) and Cup (right).

Samples of the molten salts were prepared at Dynalene, Inc. by melting powders of 99.9% purity single component nitrates in their respective eutectic compositions together, and allowing the eutectic to solidify. The mixture was then broken into small pieces for ease of handling. Before any viscosity testing was performed, a 40 mL sample of salt was placed in the couette fixture before closing the furnace. The furnace was set to a temperature above the melting point, typically 30-40°C higher, and allowed to melt into its liquid state for 30 minutes. Once the sample was visually inspected to be completely melted, the testing protocol was commenced. The testing protocol for viscosity data as a function of temperature are contained in Table 1 below:

Step	Procedure
1	Let 40 mL molten salt sample thermally equilibrate to desired testing temperature for 15 minutes.
2	Open furnace door; lower couette spindle into fluid, creating meniscus of fluid between two interfaces.
3	Close furnace door; let sample thermally equilibrate again for 2 minutes.
4	Verify furnace temperature has balanced with desired testing temperature.
5	Run test; 4 different shear rates are sampled during each run, 50, 75, 100, and 125 Hz, with each shear rate running for 10 seconds.
6	Once test is completed, record data into spreadsheet.
7	Increment temperature to next desired temperature.

Table 1: Rheometer operation procedure for molten salt viscosity data collection.

Sample images detailing the fixture, the furnace, and a proper meniscus are shown below (Figure 3A-B, Figure 4).

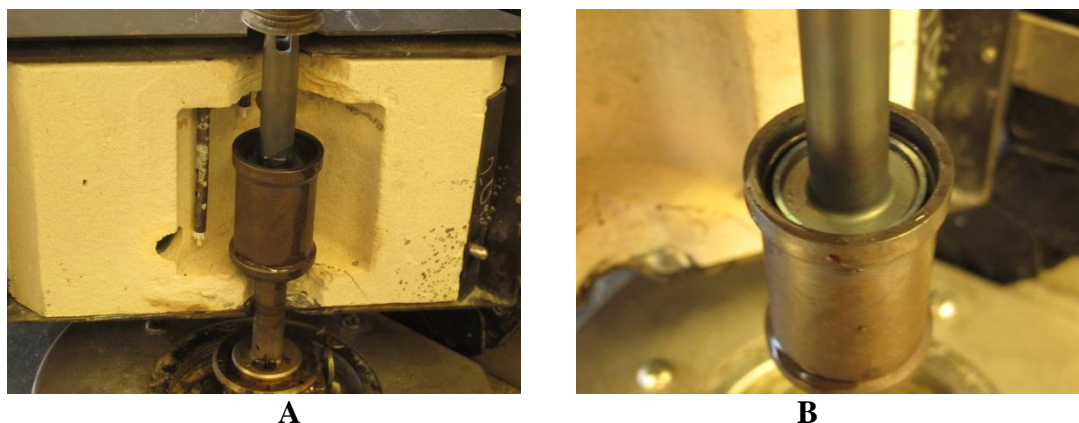


Figure 3: A) Couette Fixture mounted with open furnace door. B) Detail view of proper meniscus prior to testing.

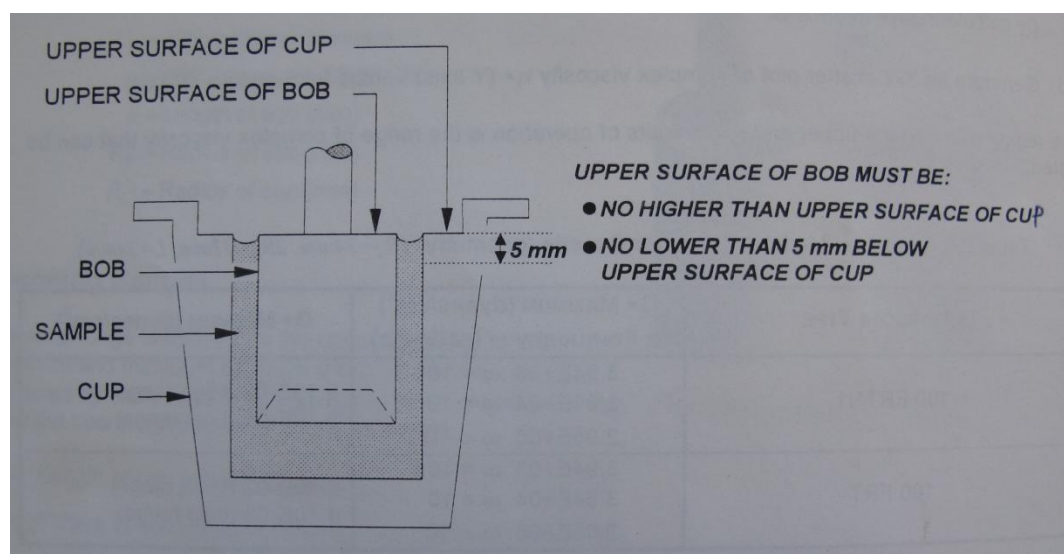


Figure 4: Schematic detailing proper meniscus position in relation to cup.

The testing protocol for viscosity data as a function of shear rate is tabulated below (Table 2):

Step	Procedure
1	Let 40 mL molten salt sample thermally equilibrate to desired testing temperature for 15 minutes.
2	Open furnace door; lower couette spindle into fluid, creating meniscus of

	fluid between two interfaces.
3	Close furnace door; let sample thermally equilibrate again for 2 minutes.
4	Verify furnace temperature has balanced with desired testing temperature.
5	Run test; test many different shear rates from 10 to 1000 Hz in log increments, with each shear rate running for 10 seconds.
6	Once test is completed, record data into spreadsheet.

Table 2: Shear Thinning test procedure for molten salt viscosity data collection.

Because the dimensions of the spindle and cup are known, along with the shear rate applied during the test, the rheometer is able to calculate the viscosity of the fluid at a given temperature using Newton’s law of viscosity:

$$\tau = \mu \frac{\partial u}{\partial x} \quad (3.1)$$

where τ represents the shear stress, $\frac{\partial u}{\partial x}$ represents the change in velocity across the thickness of the fluid, and μ represents the viscosity of the fluid.

The thermal conductivity testing protocol was similar to that of the viscosity testing and is outlined below:

Step	Procedure
1	Place 40 mL solid molten salt in base (cup) of thermal conductivity cell; place cell base inside furnace.
2	Carefully run lead wires out the top of the oven through inlet/outlet hole.
3	Turn on furnace to desired temperature for rapid melting, typically 30-40°C above the melting point for the eutectic mixture.
4	Let sample melt for 30 minutes.
5	Open furnace door; visually inspect sample is fully melted.
6	Place testing cap on top of cell base, ensuring platinum wire is fully submerged in molten salt.
7	Close furnace door; allow sample to thermally equilibrate to desired testing temperature for 2 minutes.

8	Verify furnace temperature has balanced with desired testing temperature.
9	Run test
10	Record data into spreadsheet.
11	Increment temperature to next desired testing temperature.

Table 3: Thermal Conductivity test procedure for molten salt data collection.

Because the heat input into the platinum wire is known in addition to the dimensions of the cell, the specific heat capacity of the molten salt, and Euler's constant, the relation for temperature change of a thin line heat source in an infinite medium can be used:

$$\Delta T = \frac{q}{4\pi\lambda(T, P)} \ln \frac{4\kappa t}{r^2 C} \quad (3.2)$$

where ΔT represents the temperature change in the wire ($^{\circ}\text{C}$), q represents the heat generated via joule heating per unit volume in the wire (W/m^3), r represents the radius of the platinum wire, C represents Euler's constant, α represents the thermal diffusivity of the fluid (m^2/s), t represents time in seconds, and $\lambda(T, P)$ represents the thermal conductivity of the fluid, noting it is a function of the temperature as well as the pressure of the fluid.

The above equation is valid only when $r^2/4\alpha t \ll 1$ is satisfied. The temperature rise ΔT as a function of time is calculated by relating the known current flowing through the circuit to the resistance of the wire (which is changing as a function of time), and relating to the electrical resistivity as a function of temperature characteristics of the metals involved in the circuit. By analyzing the slope of the linear portion of the ΔT vs. $\ln(t)$ curve, here denoted as S, the thermal conductivity can be calculated as:

$$\lambda(T, P) = \frac{q}{4\pi S} \quad (3.3)$$

A LABView virtual instrument was modified from an existing template created by Keithley Instruments. The current applied to the platinum wire can be changed as well as the time the current is applied for. Following each run, the script exports the resistance data for further analysis.

4: Design and Fabrication

The thermal conductivity cell was designed using SolidWorks and ANSYS software packages for 3D CAD modeling and thermal simulation. The design parameters used to develop the cell were:

No.	Parameter	Variable
1	Platinum wire temperature rise $\sim 5^{\circ}\text{C}$	$\Delta T_{\text{minimum}} = 5^{\circ}\text{C}$
2	Heat pulse time less than 30 seconds	$t_{\text{pulse}} < 30$
3	Applied electrical current < 1 Ampere	$I_{\text{heat}} < 1 \text{ A}$
4	Hold significant sample volume	$V_{\text{minimum}} = 80 \text{ mL}$
5	Avoid corrosion at high temperatures	N/A
6	Provide measurable resistance and voltage signals	$\Delta V \sim 5\text{-}10 \mu\text{V}$

Table 4: Major design parameters for thermal conductivity cell.

In order to satisfy the above design requirements, the dimensions of the platinum wire, the inner diameter of the cell, and the cell height were varied to achieve the necessary 5°C temperature differential in the platinum wire.

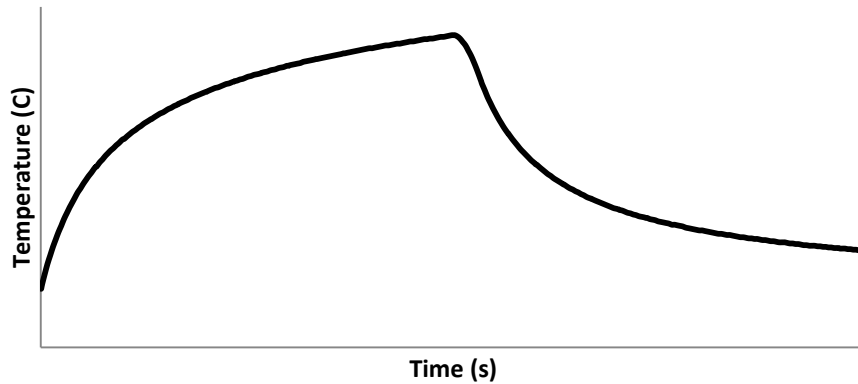


Figure 5: Schematic showing temperature profile of wire heating, plotting Temperature ($^{\circ}\text{C}$) vs. Time (s).

A logarithmic relationship between the wire temperature and the heating time at a constant current was observed, implying the nominal temperature increase for every extra second of heating after 10 seconds was less than for the second prior (Figure 5).

It was observed that the necessary temperature rise of 5°C was only attainable for a current < 1 Amp if the platinum wire diameter were exceptionally small, on the order of ~125 µm or less. Due to the brittle nature of a wire with such a small diameter, the < 1 Amp current ceiling was lifted in favor of using a larger, more structurally stable wire capable of delivering the desired temperature increase. Therefore, a 500 µm wire diameter was shown to be ideal in matching the required temperature increase with structural stability when subjected to a current of ~5 Amps. The higher current translates into the need for more expensive sensing equipment, and additional safety measures when operating the device.

The determination of the inner diameter of the cell was important in maintain the accuracy of the instrument. If the walls of the cell are positioned too close to the heat source, the analytical solution for the thin line heat source will break down. After simulating in ANSYS, an inner diameter of 60 mm was deemed appropriate to allow the salt to behave as an infinite medium.

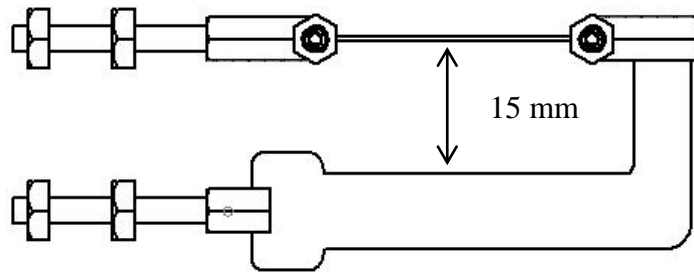


Figure 6: 2D CAD drawing (side view) of platinum wire and stainless steel bracket arm.

This implies the distance to the cell wall from the platinum wire is 30 times the diameter of the wire itself. With the bracket arm being the next closest potential heat source, it was designed to be at least 15 mm away (radially) from the platinum wire, leaving at least 15 times the radius of wire to act as the “infinite” medium (Figure 6).

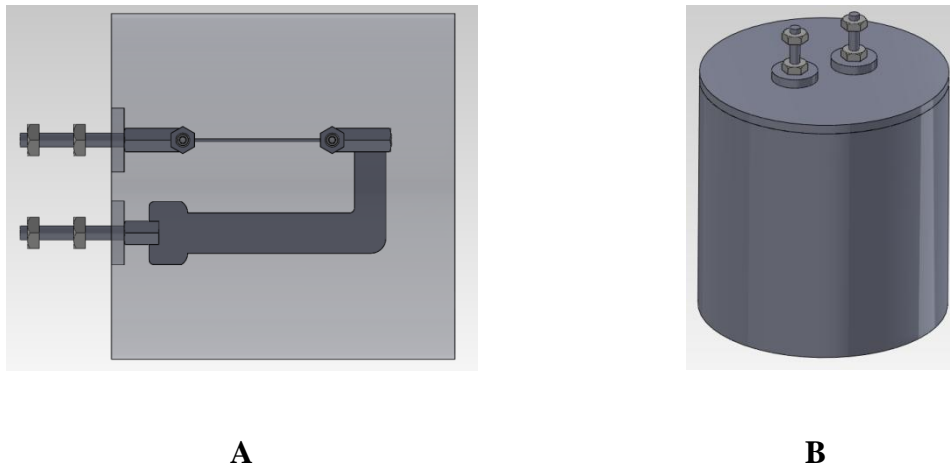


Figure 7: 2D CAD drawing of device circuit and base, A) transparent, and B) assembled.

The wire was held in place using an L-shaped arm, allowing the arm to be sufficiently far away from the platinum wire so as not to allow any significant heat transfer to occur and cause error in the results (Figure 7).

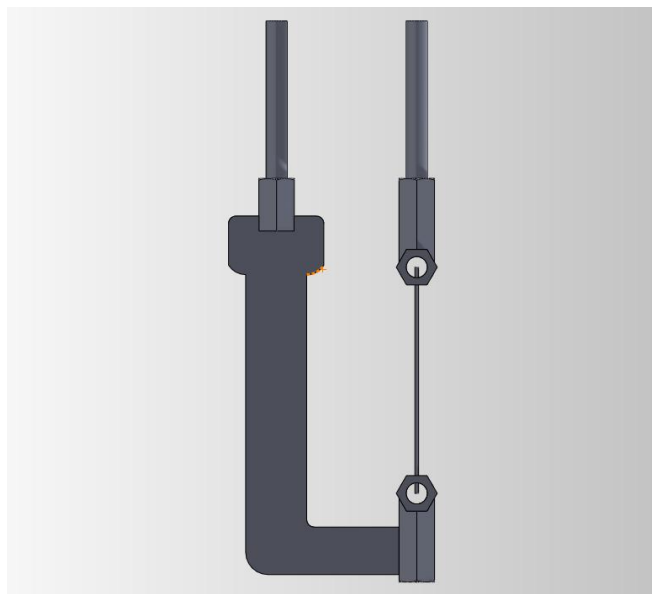


Figure 8: Close up view of L-shaped bracket.

The entire cell was designed with the effects of high temperature corrosion in mind. Consequently, the cell base, cap, and arm were machined from Stainless Steel 316L. The wire was made from 1 mm diameter 99.9% Platinum, and secured to the arm and cap using a drill and tap. The entire cap is removable in order to allow easy and efficient sample loading and unloading. Additionally, it allows the platinum wire to be completely submerged in the molten salt, preventing an error due to air pockets. Electrical insulation between the platinum wire and the cap was achieved using a high temperature ceramic insert (Figure 8, Figure 9).

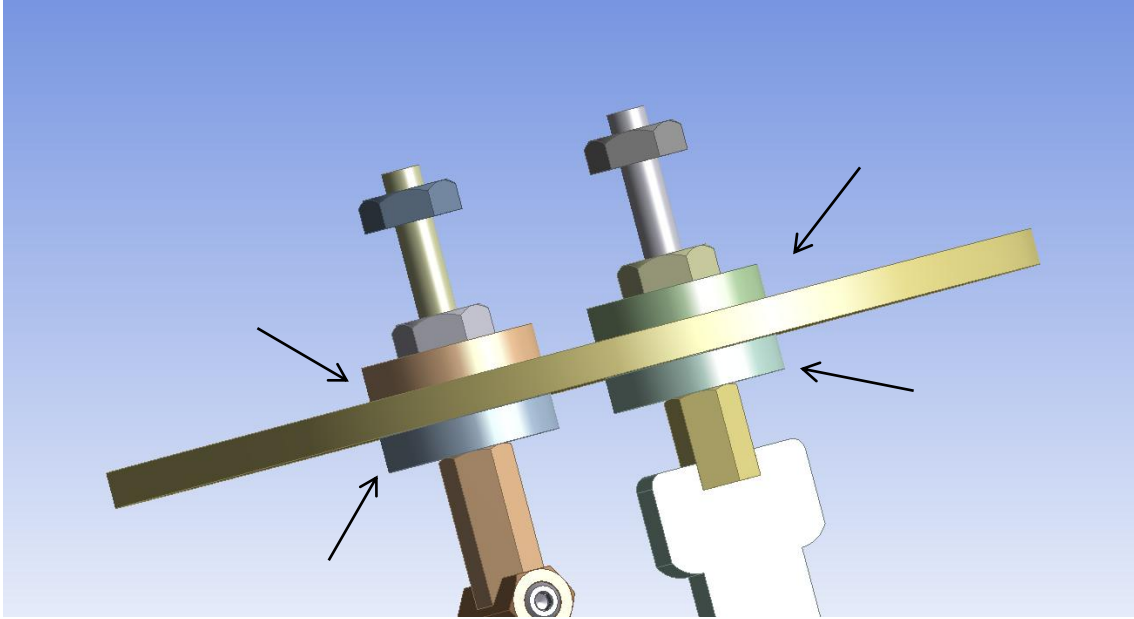


Figure 9: Close-up view of mechanical and electrical contacts between cap, bracket, and wire.

While the testing using this thermal conductivity cell was limited to proof-of-concept using well known, fully characterized control fluids, the device was designed to operate at the high temperatures required for the molten alkali-nitrate salts (Figure 9). The ceramic inserts are highlighted in Figure 9 to illustrate the electrical isolation achieved between the circuit and the stainless steel cap. The entire electrical circuit is completed as a Keithley Instruments Sourcemeter and Nanovoltmeter are connected via a set of four copper lead wires to the stainless steel bit and the stainless steel arm which are threaded through the cell cap. Between the stainless steel joiner and the arm is the platinum wire, which completes the circuit. The sourcemeter is connected to a GPIB card which connects to the computer interface (LabVIEW) for data collection.

A full view of the CAD model design, Figure 10, is included for reference.

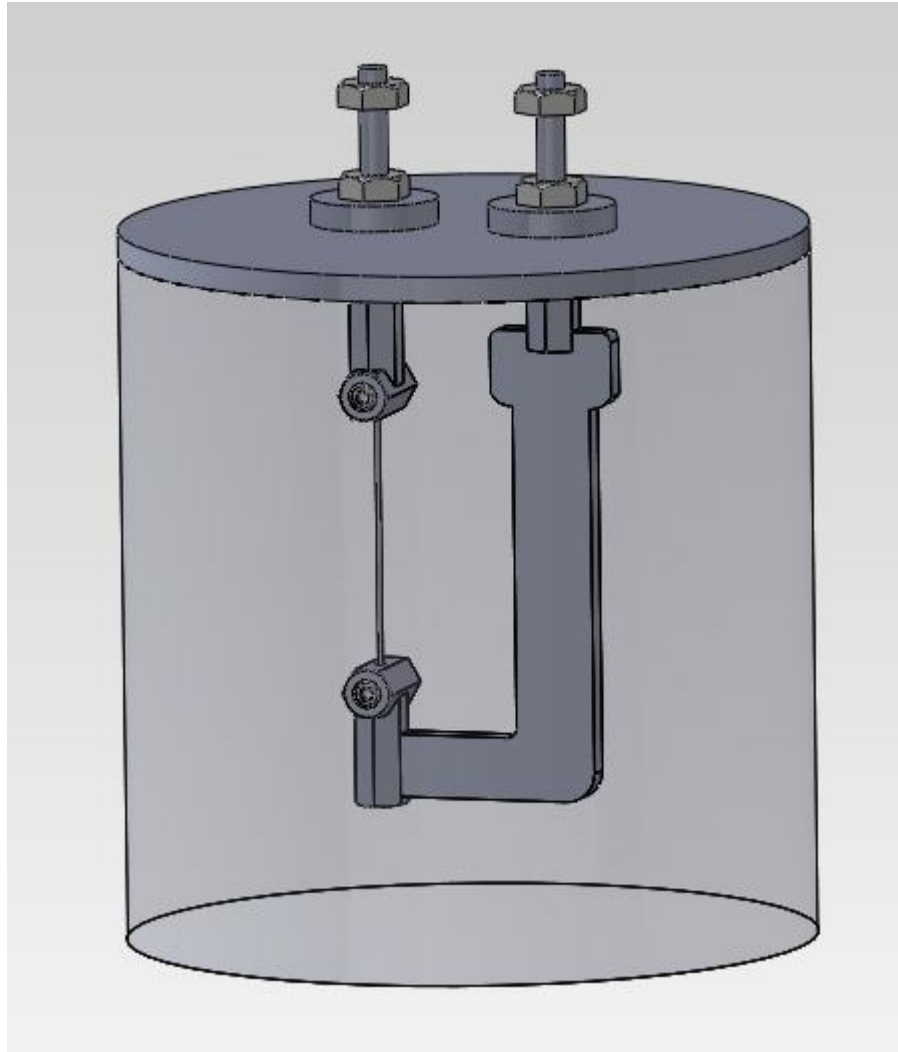


Figure 10: 3D CAD drawing of thermal conductivity device.

5: Thermal Analysis

5.1: Pressure Drop and Heat Loss Simulation of CSP Night Operation

In conjunction with the design of the thermal conductivity cell, heat transfer and fluid dynamics analysis of the different molten alkali-nitrate salts flowing through a sample parabolic trough concentrating solar power plant at night when no power is being generated was performed. It was hypothesized that the lower melting temperature and thus lower minimum operating temperature of the ternary LiNaK-NO₃ eutectic would result in a greater energy savings via reduced heat loss compared to the increased velocity associated with the lower viscosity of the system compared to the binary eutectic salts. The heat transfer analysis was carried out for a typical solar receiver outlined in Figure 11 below.

Cross Section of Solar Receiver:

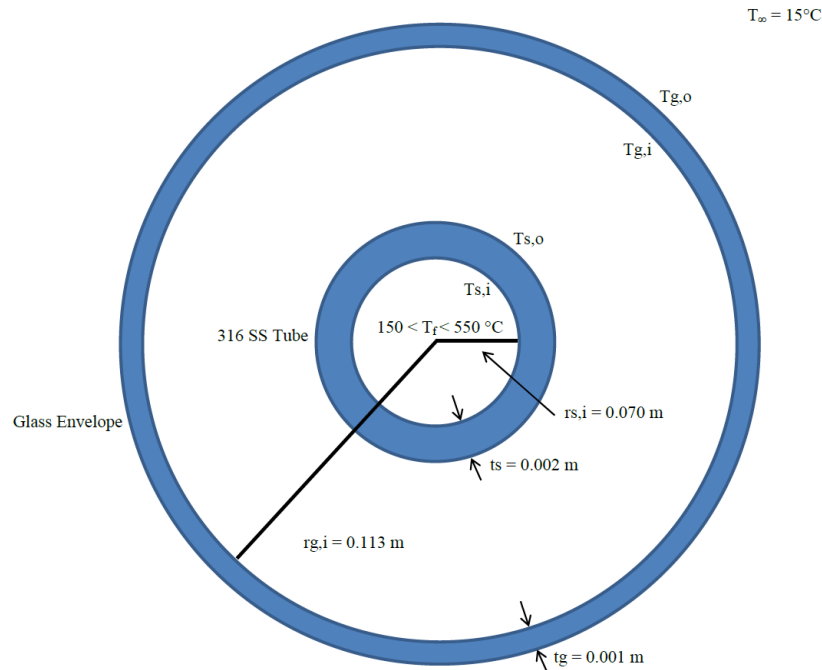


Figure 11: Solar receiver cross section.

$T_{g,o}$ refers to the temperature of the outside of the glass envelope, $T_{g,i}$ refers to the temperature of the inside of the glass envelope, $T_{s,o}$ refers to the temperature of the outside of the solar receiver, $T_{s,i}$ refers to the temperature of the inside of the solar receiver. $r_{s,i}$ refers to the inner radius of the solar receiver which is 0.070 m, $t_{s,o}$ refers to the thickness of the solar receiver wall which is 0.002 m, t_g refers to the thickness of the glass envelope, which is 0.001 m. The ambient temperature outside the envelope is 15°C, and the temperature of the fluid, T_{fluid} varies between 150 and 550°C.

The assumptions made for this analysis were steady state heat transfer, turbulent flow in the pipe, and fully developed flow. Consequently, the convection and radiation to the atmosphere must balance with the conduction through the glass, the radiation through the vacuum (between the inner surface of the glass envelope and the outer surface of the steel pipe), the conduction through the steel pipe, and the convection from the heat transfer fluid. This is expressed using conservation of energy in equation 5.1.1.

$$\begin{aligned} Q_{conv, HTF'} &= Q_{cond, steel'} = Q_{rad, vac'} = Q_{cond, glass'} \\ &= Q_{conv, out'} + Q_{rad, out'} \end{aligned} \quad (5.1.1)$$

Using Fourier's Law and Newton's Law of Cooling this can be rewritten as:

$$\begin{aligned} 2\pi r_s h_{forced}(T_{s,i} - T_{fluid}) &= \frac{2\pi k_s(T_{s,o} - T_{s,i})}{\ln\left(\frac{r_s + t_s}{r_s}\right)} = (2\pi\sigma r_g(T_{g,i}^4 - T_{s,o}^4)) / \left(\frac{1}{\epsilon_s} + \right. \\ \left. \left(\frac{1 - \epsilon_g}{\epsilon_g}\right) \left(\frac{r_s}{r_g}\right)\right) &= \frac{2\pi k_g(T_{g,o} - T_{g,i})}{\ln\left(\frac{r_g + t_g}{r_g}\right)} = 2\pi\sigma\epsilon_g(r_g + t_g)(T_{g,o}^4 - T_{\infty}^4) + h_{free}2\pi r_g(T_{g,o} - \\ &T_{\infty}) \end{aligned} \quad (5.1.2)$$

where h_{forced} represents the convection coefficient associated with the flow of fluid pumped through the inner radius of the pipe in (W/m^2), k_s represents the thermal conductivity of the steel pipe ($W/m K$), ϵ_g represents the emissivity of the glass envelope, ϵ_s represents the emissivity of the steel pipe, σ represents the Stefan-Boltzmann constant defined as 5.670373×10^{-8} ($W m^{-2} K^{-4}$), h_{free} represents the convection coefficient of free convection occurring on the glass envelope outer surface (W/m^2), and T_∞ represents the temperature of the ambient air surrounding the glass envelope (K).

The temperatures were non-dimensionalized to aid in the analysis by declaring $\theta_n = \frac{T_n}{T_\infty}$. The above equation thus simplifies to:

$$\begin{aligned}
2\pi r_s h_{forced} \left(\theta_1 - \frac{T_{fluid}}{T_\infty} \right) T_\infty &= \frac{2\pi k_s (\theta_2 - \theta_1)}{\ln \left(\frac{r_s + t_s}{r_s} \right)} \\
&= (2\pi \sigma r_g (\theta_3^4 - \theta_4^4) T_\infty^4) / \left(\frac{1}{\epsilon_s} + \left(\frac{1 - \epsilon_g}{\epsilon_g} \right) \left(\frac{r_s}{r_g} \right) \right) = \frac{2\pi k_g (\theta_4 - \theta_3)}{\ln \left(\frac{r_g + t_g}{r_g} \right)} \quad (5.1.3) \\
&= 2\pi \sigma \epsilon_g (r_g + t_g) (\theta_4^4 - 1) T_\infty^4 + h_{free} 2\pi r_g (\theta_4 - 1) T_\infty
\end{aligned}$$

Fluid velocity and heat transfer were related via the Nusselt and Reynolds numbers for turbulent flow. The Nusselt number for forced convection, here defined as Nu_D represents the ratio of convective to conductive heat transfer normal to the diameter of the steel pipe and is calculating from h_{forced} , $r_{s,o}$ (the pipe radius), and k_s (the pipe thermal conductivity).

$$Nu_D = \frac{2h_{forced}r_{s,o}}{k_s} = \frac{\left(\frac{f}{8}\right)(Re_D - 1000)Pr}{1 + 12.7\left(\frac{f}{8}\right)^{\frac{1}{2}}(Pr^{\frac{2}{3}} - 1)} \quad (5.1.4)$$

Equation 5.1.4 is valid for forced convection in steel pipe over a range of $0.5 < Pr < 2000$ and $10,000 < Re < 5,000,000$. The Darcy friction factor of the pipe, here defined as f , represents the friction losses in closed pipe flow. It is represented in two forms depending on the flow scenario below:

Laminar:

Turbulent:

$$f = 64/Re_D \quad \frac{1}{\sqrt{f}} = -2\log_{10}\left(\frac{\epsilon}{3.7D_h} + \frac{2.51}{Re\sqrt{f}}\right) \quad (5.1.5)$$

Equation 5.1.5 is valid for $Re > 4000$. ϵ represents the roughness height (m), and D_h represents the hydraulic diameter (m).

The Reynolds number of the flowing HTF, here defined as Re_D , represents the ratio of inertial forces to viscous forces occurring within the steel pipe and is calculated using the properties of the HTF, ρ_{fluid} , the density of the fluid (kg/m^3), v_{fluid} , the characteristic speed, in this case the velocity of the fluid (m/s), μ_{fluid} , the viscosity of the fluid (Poise) and $r_{s,i}$, the inner diameter of the pipe (m).

$$Re_D = 2\frac{\rho_{fluid}v_{fluid}r_{s,i}}{\mu_{fluid}} \quad (5.1.6)$$

The Prandtl number of the flowing HTF, here defined as Pr , represents the ratio of kinematic viscosity to thermal diffusivity and is calculated using the properties of the HTF, ν_{fluid} , the kinematic viscosity of the fluid (m^2/s) and α_{fluid} , the thermal diffusivity of the fluid (m^2/s).

$$\text{Pr} = \frac{\nu_{fluid}}{\alpha_{fluid}} \quad (5.1.7)$$

The Nusselt number for free convection is defined below as Nu_{free} , representing the ratio of convective to conductive heat transfer normal to the diameter of the outer glass envelope:

$$\sqrt{Nu_{free}} = \sqrt{\frac{2h_{free}r_{g,o}}{k_g}} = 0.90 + 0.387 \left[\frac{Ra}{\left\{1 + \left(\frac{0.559}{Pr}\right)^{9/16}\right\}^{16/9}} \right]^{1/6} \quad (5.1.8)$$

for free convection to ambient air. The Rayleigh number, here defined as Ra , represents the relationship between density forces and viscous forces in the ambient air.

$$Ra = \frac{g\beta(T_{g,o} - T_{\infty})D_{g,o}^3}{\nu_{air}\alpha_{air}} \quad (5.1.9)$$

where g represents the acceleration due to gravity (m^2/s), β represents the thermal expansion coefficient by volume of the ambient air ($1/^{\circ}\text{C}$), ν_{air} represents the kinematic viscosity of the ambient air (m^2/s), and α_{air} represents the thermal diffusivity of the ambient air (m^2/s). The pressure drop in the solar receiver was calculated using the friction factor of the pipe and the fluid velocity with the following relation:

$$\Delta P = \rho_{fluid} \left(\frac{fLv_{fluid}^2}{4r_{s,i}} \right) \quad (5.1.10)$$

where ΔP represents the pressure drop in the pipe (Pa), ρ_{fluid} represents the density of the fluid inside the pipe, L represents the length of the pipe (m), and v_{fluid} represents the fluid velocity (m/s).

A MATLAB script was written to carry out the simultaneous solution of these equations. The necessary thermo-physical properties were estimated based on the

HITEC XL molten salt (48:45:7 $\text{Ca}(\text{NO}_3)_2\text{-KNO}_3\text{-NaNO}_3$), a closely similar compound compared to the binary and ternary eutectic salts of interest to the present work.

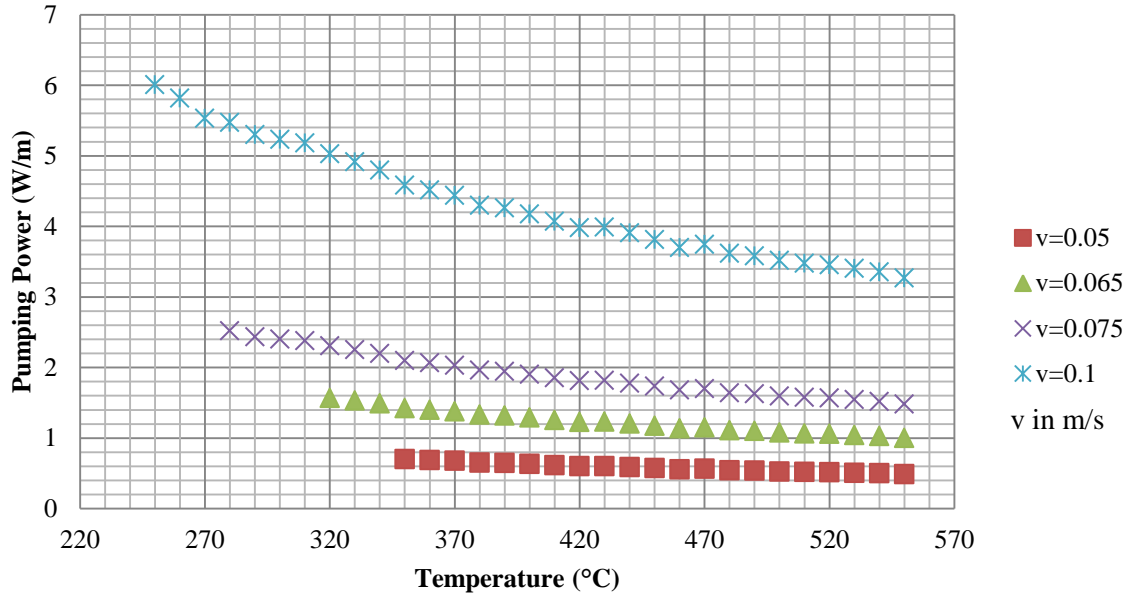


Figure 12: Pumping Power (W/m) vs. Temperature (°C) for LiNaK-NO₃.

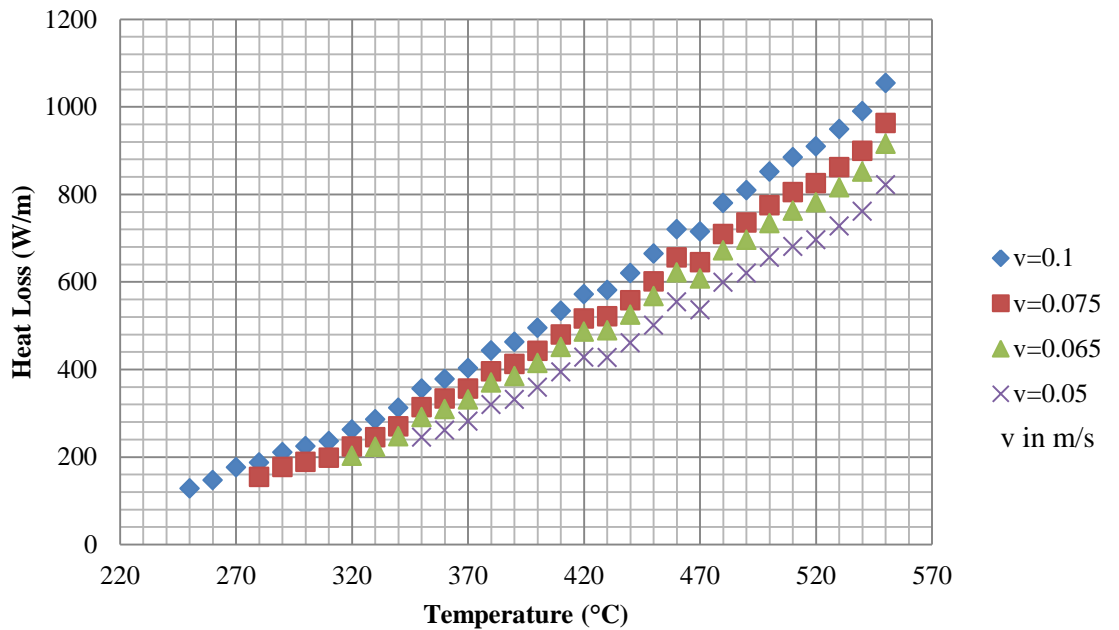


Figure 13: Heat Loss (W/m) vs. Temperature (°C) for LiNaK-NO₃.

The figures above display the pumping power, in W/m, required to circulate LiNaK eutectic molten salt through a 1 m section of pipe at several different velocities (Figure 12), and the heat loss, in W/m, occurring through the same length of pipe (Figure 13). Upon comparison of the two figures, it is clear the heat loss associated with a 0.1 m/s flow rate at 250°C is 130 W/m, compared to 6 W/m pumping power. Consequently, the goal of minimizing energy input or losses when not generating power is best achieved by selecting a salt which can operate at as low a temperature as possible while remaining molten, in order to avoid the large energy losses associated with the loss of heat to the surrounding environment. In the context of the present work, this trend suggests using the LiNaK-NO₃ ternary eutectic molten salt as a heat transfer fluid over any of the binary mixtures due to its expanded operating range. The lower the melting temperature of the heat transfer fluid, the more practical it is to avoid significant energy loss. During hours of the day when the plant is generating power it is paramount to select a fluid which can run at as high a temperature as possible in order to produce the highest quality steam and increase Rankine efficiency.

5.2: Thermal Conductivity Cell Finite Element Simulations

Using the ANSYS transient thermal package, a transient, three-dimensional numerical simulation of the thermal conductivity device was carried out. The conditions of the simulations were as follows: initially, the device and the salt are thermally equilibrated at 550°C. No convective or radiative boundary conditions are applied to ensure the only mode of heat transfer present is via conduction. To simulate joule heating due to the 5A current run through the circuit, an internal heat generation boundary condition is applied to all nodes within the platinum wire, the L-shaped bracket, and any other metal surfaces through which a current is carried. This heat generation condition is applied only for the first 15 seconds of measurement. A further 15 seconds are simulated to observe the effects of heat dissipation from the wire to the salt medium.

The governing equation for this numerical simulation is Fourier's Law of heat conduction in three dimensions, presented below:

$$\rho_w C_{p,w} \frac{\partial T}{\partial t} = \dot{q} + \frac{\partial}{\partial x} \left(k_w \frac{\partial T}{\partial x} \right) + \frac{\partial}{\partial y} \left(k_w \frac{\partial T}{\partial y} \right) + \frac{\partial}{\partial z} \left(k_w \frac{\partial T}{\partial z} \right) \quad (5.2.1)$$

where ρ_w represents the density of the wire (kg/m^3), $C_{p,w}$ represents the specific heat capacity of the wire (J/g C), k_w represents the thermal conductivity of the wire (W/m K), $\frac{\partial T}{\partial x}$, $\frac{\partial T}{\partial y}$, $\frac{\partial T}{\partial z}$ represent the change in temperature in each of the three axial ordinates, and t represents time in seconds. The simulation also applies Fourier's Law of heat conduction in three dimensions, without a heat generation term, to the stationary fluid.

$$\rho_{fluid} C_{p,fluid} \frac{\partial T}{\partial t} = \frac{\partial}{\partial x} \left(k_{fluid} \frac{\partial T}{\partial x} \right) + \frac{\partial}{\partial y} \left(k_{fluid} \frac{\partial T}{\partial y} \right) + \frac{\partial}{\partial z} \left(k_{fluid} \frac{\partial T}{\partial z} \right) \quad (5.2.2)$$

Continuous temperature and heat flux boundary conditions are applied at the interface of the fluid and the wire:

$$r \rightarrow r_w \quad T_w = T_{fluid} \quad (5.2.3)$$

$$r \rightarrow r_w \quad -k_w \frac{\partial T}{\partial n} = -k_{fluid} \frac{\partial T}{\partial n} \quad (5.2.4)$$

where $\frac{\partial T}{\partial n}$ represents the change in temperature in each of the axial ordinates x, y, and z.

The heat generation in the various complex geometries such as the hexagonal hollow cylinders and the L-shaped bracket arm is not represented analytically here, but was accounted for by incorporating the resistance of each geometry into the simulation and determining the magnitude of joule heating from the product of the square of the applied current and the known resistance.

As the thermal conductivity device was simulated during the design process, the sensitivity of the Temperature vs. time profile was analyzed with respect to two variables: mesh size, and time step. The different meshes are shown below (Figure 14). Due to the varied geometries involved in this solid model, both quadrilateral and triangular mesh shapes were utilized. For example, the bracket arm geometry uses triangular element shapes, while the platinum wire makes use of quadrilateral elements. Quadratic shell elements were applied to the mesh to better fit the irregular geometries present.

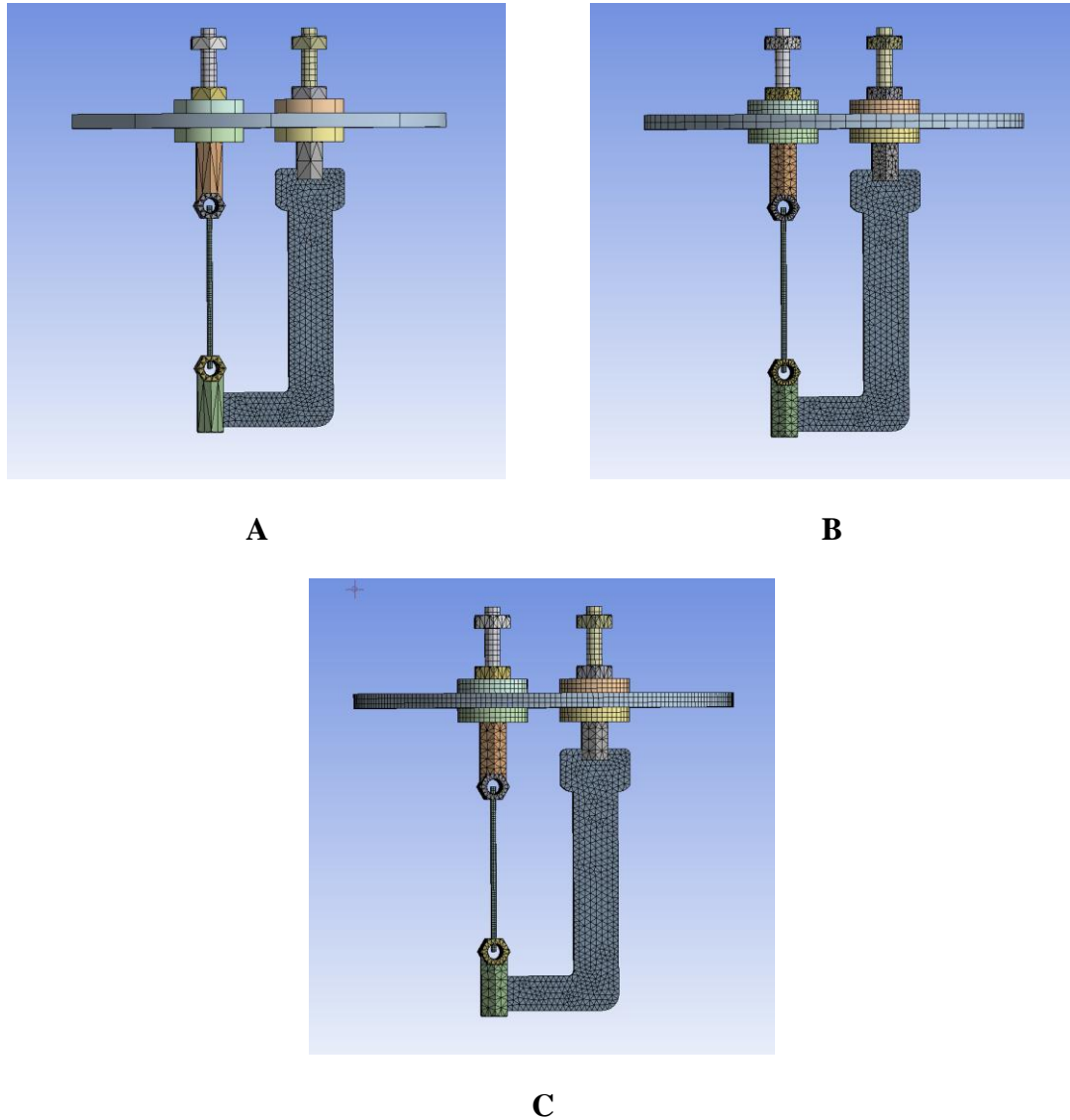


Figure 14: A) Coarse B) Medium and C) Fine Mesh Geometries used in Transient Thermal analysis using ANSYS

Each transient thermal simulation was run for the same set of conditions with the system initially at 550°C , before the application of a current of 5 Amps applied over 15 seconds. The wire is left to cool for an additional 15 seconds before measurement stops. First, the simulation's dependence on varying mesh sizes was analyzed by

altering the meshing between coarse, medium, and fine settings while keeping the time step size constant at 0.01 seconds.

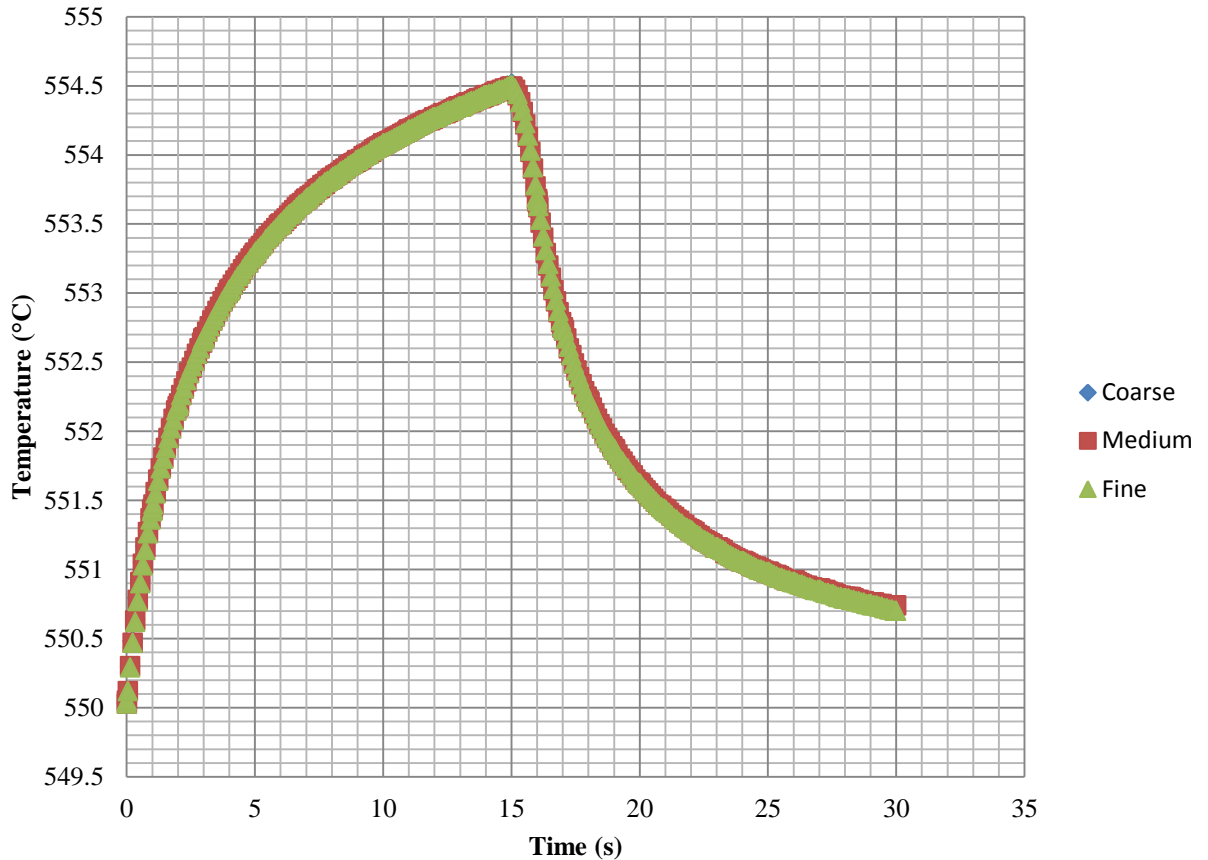


Figure 15: Temperature (°C) vs. Time (s) for 1 mm Platinum Wire. Three different mesh sizes were tested and plotted: coarse, medium, and fine.

The simulation showed only minute variation in the temperature vs. time profile of the wire as the mesh size was altered. For example, at 15 seconds, the end of the applied current and thus the end of the wire’s heating period, the temperature was projected to reach 554.51°C with the coarse mesh, 554.49°C with the medium mesh, and 554.50°C with the fine mesh (Figure 15). This data suggests the simulation is a

robust and accurate solution for the behavior of the platinum wire when under the applied conditions.

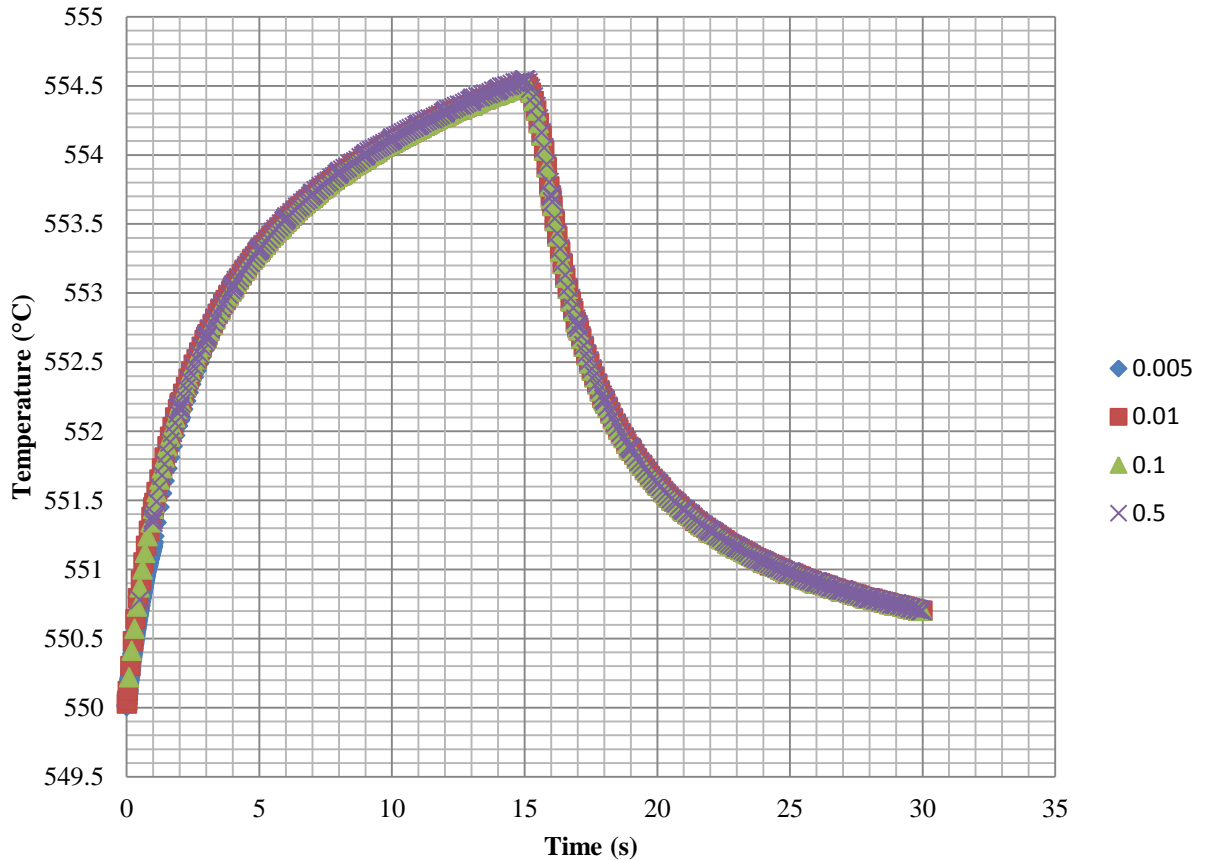


Figure 16: Temperature (°C) vs. Time (s) for 1 mm Platinum Wire. Four different time step sizes were tested and plotted: 0.005, 0.01, 0.1, and 0.5.

While it is possible for the simulation results to vary based on different mesh sizes, due to potential divergence in the mathematical model, it is also possible for the solution to diverge as a result of invalid time steps. Consequently, four different time steps were selected to analyze any changes in the simulation results. The effect of changing the time step size on the simulation output was negligible (Figure 16). At 15 seconds, the end of the heating period, the simulated temperature was reported to be

554.50°C with a 0.005 s time step, 554.51°C with a 0.01 s time step, 554.51°C with a 0.1 s time step, and 554.54°C with a 0.5 s time step. While the time step changed two orders of magnitude, the simulation results deviated a maximum of 0.04°C. This data further suggests the simulation is an accurate solution for the behavior of the platinum wire when under the applied conditions.

Given the thermal analysis for the CAD model is robust and stable, the results can be applied towards the development of the calibration script for the thermal conductivity device.

6: Calibration

6.1: Analytical Solution for Thin Line Heat Source

In conjunction with the present work, an analytical solution to the transient thin line heat source in an infinite medium was carried out resulting in a calibration procedure for determining the thermal conductivity of test fluids using resistance data collected during the heating of the platinum wire as a function of time¹⁸. This is expressed mathematically as:

$$\frac{\partial^2 T(r, t)}{\partial r^2} + \frac{1}{r} \frac{\partial T(r, t)}{\partial r} = \frac{1}{\alpha} \frac{\partial T(r, t)}{\partial t} \quad (6.1.1)$$

where r represents distance (m) in radial coordinates, α represents the thermal diffusivity of the fluid (m²/s), t represents time in seconds, $\frac{\partial T(r, t)}{\partial t}$ represents the change in temperature with respect to time, $\frac{\partial T(r, t)}{\partial r}$ represents the change in temperature with respect to radial distance, and $\frac{\partial^2 T(r, t)}{\partial r^2}$ represents the change in the temperature change with respect to radial distance.

The one-dimensional, transient heat diffusion equation above was solved analytically resulting in a series solution expressing wire temperature as a function of time:

$$T_0 = \frac{Qr_0}{k} \left[2 \sqrt{\frac{\alpha t}{\pi r_0^2}} - \frac{1}{2} \frac{\alpha t}{r_0^2} + \frac{1}{2} \frac{\left(\frac{\alpha t}{r_0^2}\right)^{3/2}}{\sqrt{\pi}} - \frac{3}{16} \left(\frac{\alpha t}{r_0^2}\right)^2 + \frac{21}{80} \frac{\left(\frac{\alpha t}{r_0^2}\right)^{5/2}}{\sqrt{\pi}} + \dots \right] \quad (6.1.2)$$

where T_0 represents the wire temperature ($^{\circ}\text{C}$), Q represents the heat input per unit surface area of the wire (W/m^2), r_0 represents the radius of the wire (m), α represents the thermal diffusivity of the wire (m^2/s), and k represents the thermal conductivity of the wire ($\text{W}/\text{m K}$). Using the resistance to temperature calibration performed for the experimental set up, resistance data can be translated to temperature vs. time data which is analyzed using a nonlinear curve fitting method applied to the above equation.

6.2: Resistance and Temperature Calibration

The resistance of the thermal conductivity apparatus was measured as a function of temperature using distilled H₂O as a calibration fluid. Resistance data was recorded in multiple runs at 23, 50, and 55 °C and fit using a linear least squares regression to obtain an empirical relation of R(T) (Figure 17) . This relation was then used to later translate Resistance(time) data to Temperature(time) allowing the thermal conductivity, λ , to be obtained via the aforementioned procedure.

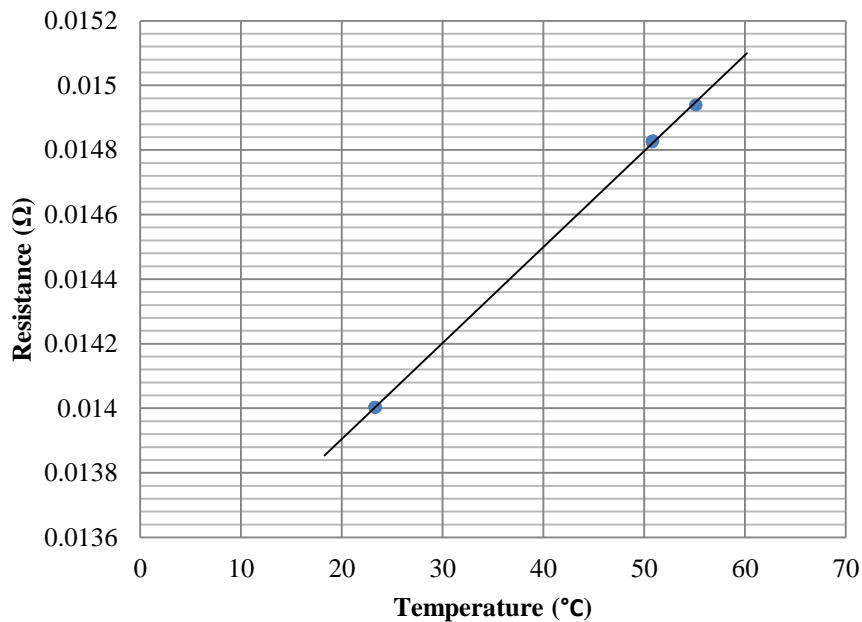


Figure 17: Resistance (Ω) vs. Temperature ($^{\circ}\text{C}$) for 1mm Platinum Wire thermal conductivity device immersed in distilled H₂O.

An example of the thermal conductivity determination is highlighted by comparing the slopes of the theoretical solution in Figure 18 below with the experimental data, which are similar over a specified time interval.

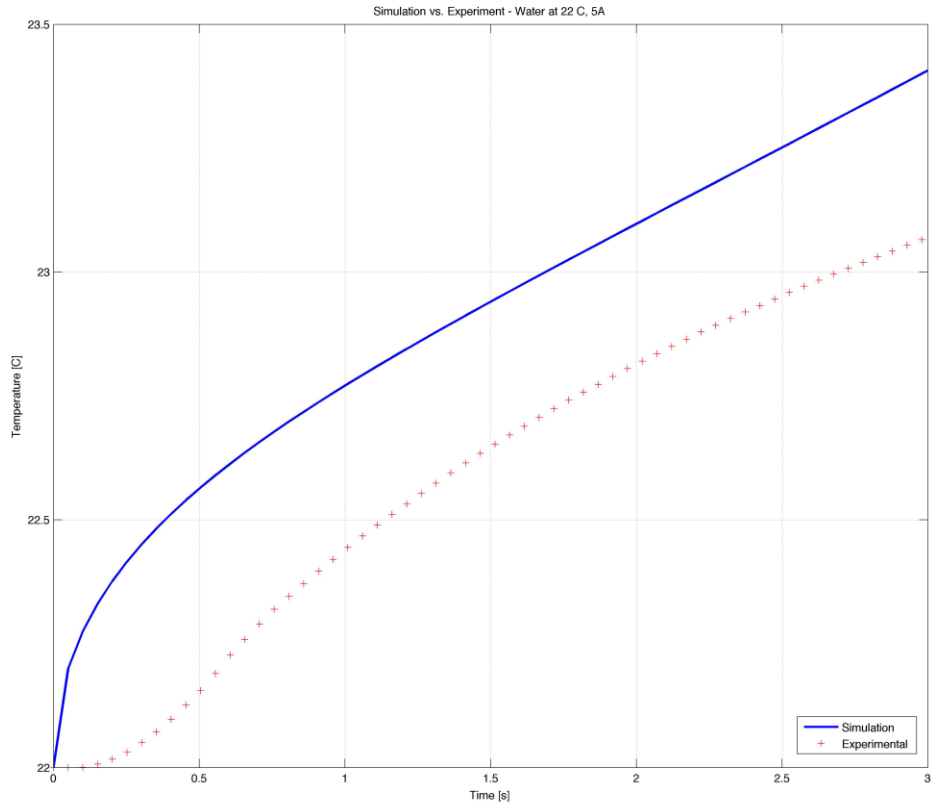


Figure 18: Temperature (°C) vs. Time (s) comparison of theoretical simulation and experimental data.

7: Results and Discussion

7.1: Viscosity

The viscosity of ternary LiNaK-NO₃ molten salt was analyzed from two aspects; first, as a potential shear thinning fluid, and second, as a function of temperature through the operating range of potential CSP plants.

Shear thinning fluids are shown to exhibit changes in viscosity at a constant temperature as the shear rate is altered. Consequently, viscosity data was collected over a range of shear rates (dynamically chosen by the TA Instruments software according to a log scale) and repeated at different temperatures (160, 250, 300, 350, and 450°C).

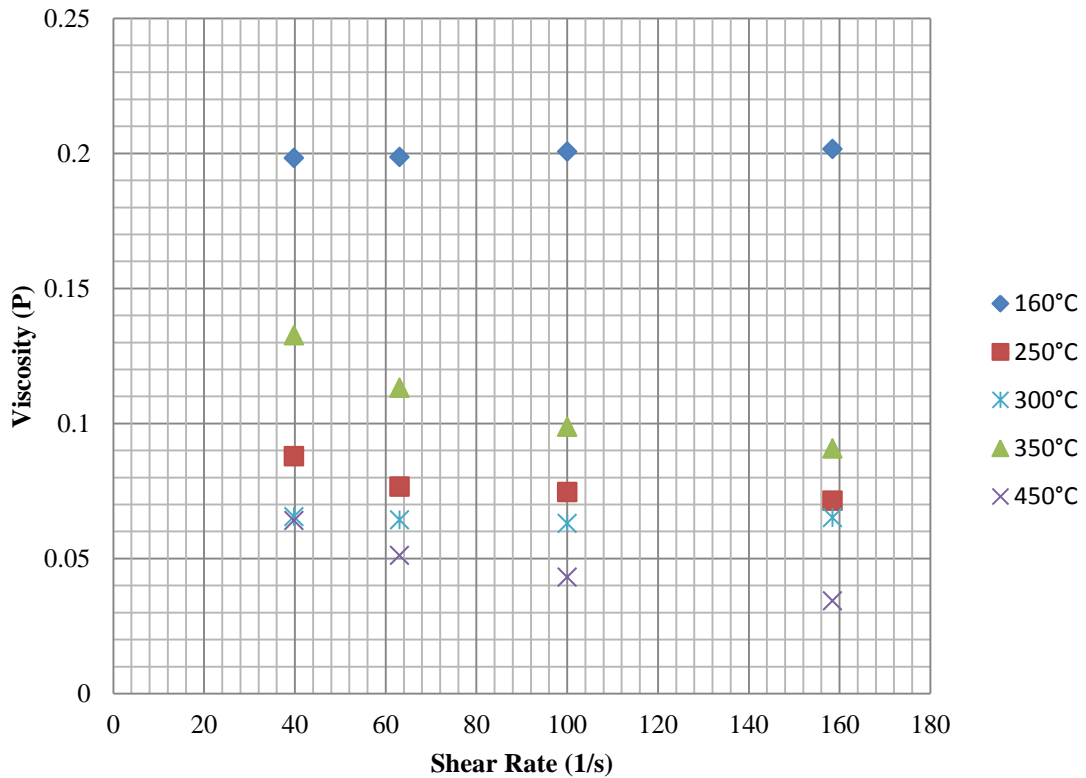


Figure 19: Viscosity (P) vs. Shear Rate (1/s) for LiNaK-NO₃ tested at 5 different temperatures, 160°C, 250°C, 300°C, 350°C, and 450°C.

The results showed no significant changes in viscosity, measured in Poise, as a function of shear rate once the shear rate at each run reached 40 Hz. Due to the low viscosity of the fluid (similar to water at elevated temperatures, approximately 1 cP), insufficient torque is measured on the ARES transducer at shear rates < 40 Hz. It is clear that once measurable torque is achieved, viscosity of the molten LiNaK-NO₃ does not vary with shear rate.

Next, the viscosities of LiNaK-NO₃, LiNa-NO₃, LiK-NO₃, and NaK-NO₃ were analyzed as a function of temperature. Typically, fluids exhibit an exponential decrease in viscosity as a function of increasing temperature, akin to:

$$\mu(T) = \mu_0 e^{-bT} \quad (7.1.1)$$

where μ_0 is the viscosity of the fluid at a reference temperature, and b is a coefficient governing the rate of decrease of viscosity with temperature. The results presented in Figure 20 verify this model. The results showed a maximum viscosity of 61 cP near the melting point of LiNaK-NO₃ (127°C) which exponentially decreased to 1.2 cP at the upper limit of the operating range of 550°C (Figure 20). NaK-NO₃ displayed a maximum viscosity of 6.88 cP at 230°C and a minimum of 1.34 cP at 550°C. LiNa-NO₃ showed a similar maximum viscosity of 6.44 cP at 240°C and a minimum viscosity of 1.33 cP at 550°C. During experiments with LiK-NO₃, the thermocouple measuring temperature in the furnace was discovered to be faulty, shifting the viscosity data to higher temperatures. Nevertheless, a maximum viscosity of 93 cP at 150°C was observed with a minimum of 1.96 cP at 550°C (Figure 20).

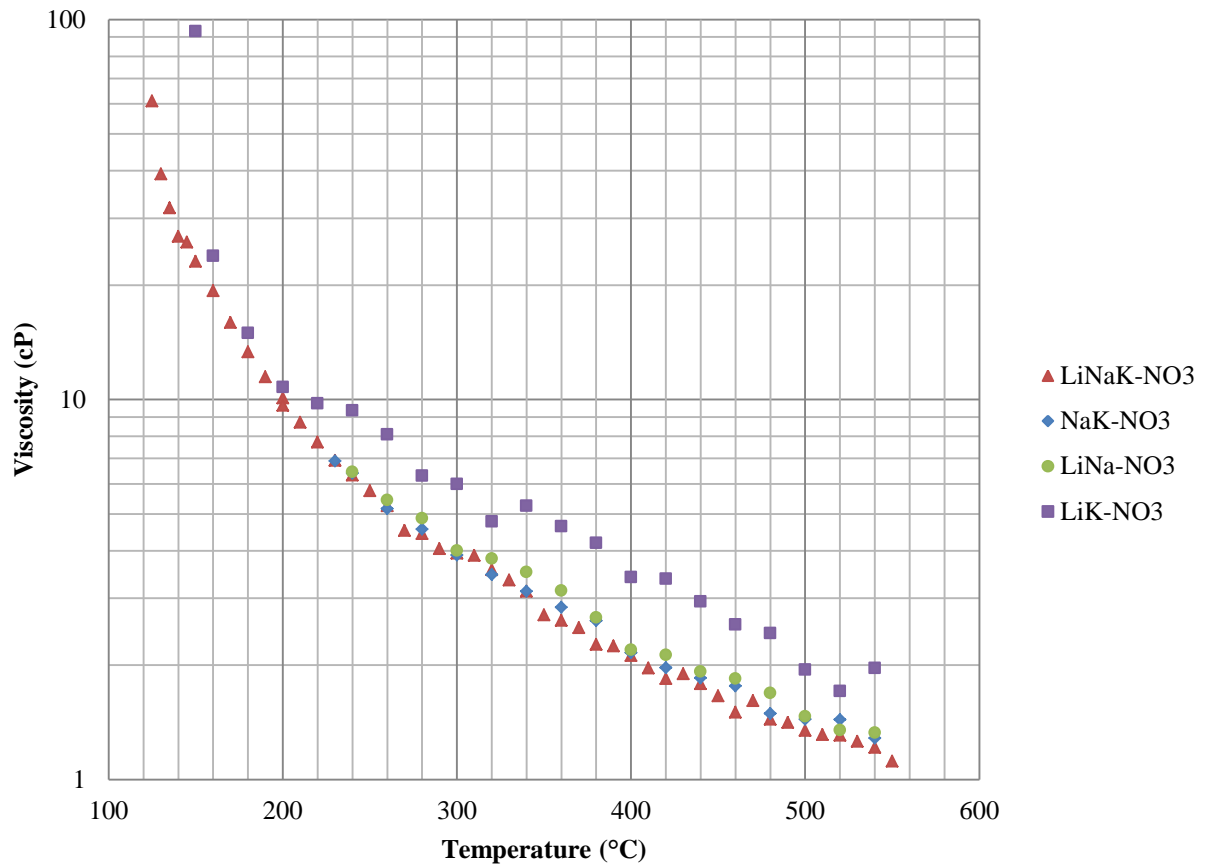


Figure 20: Viscosity (cP) vs. Temperature (°C) from melting temperature up to 550°C for four different molten salts, LiNaK-NO₃, NaK-NO₃, LiNa-NO₃, and LiK-NO₃.

The above Arrhenius model for liquid viscosity as a function of temperature was verified by comparing the activation energies of each ternary or binary molten salt with literature values. An exponential fit was performed on $\mu(T)$ data according to the Arrhenius model (a variation of the above exponential model):

$$\mu(T) = \mu_0 e^{\frac{E}{RT}} \quad (7.1.2)$$

where E represents the activation energy of the fluid and R is the universal gas constant.

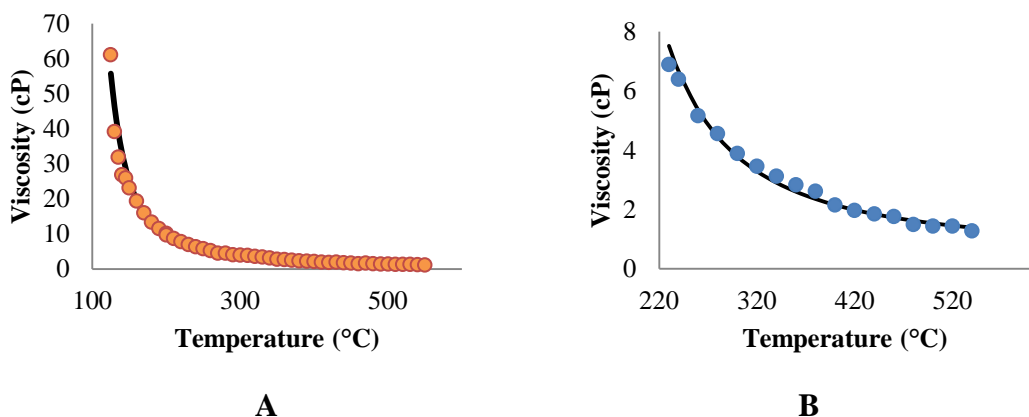


Figure 21: Viscosity (cP) vs. Temperature (°C) from melting temperature up to 550°C for A) LiNaK-NO₃ and B) NaK-NO₃ plotted with Arrhenius Fit line.

In the above figure, viscosity (cP) is shown to vary with temperature similarly with the Arrhenius fit line (black) which was constructed using an exponential fit (Figure 21). From here, activation energies were calculated for both LiNaK-NO₃ and NaK-NO₃ and compared with literature values.

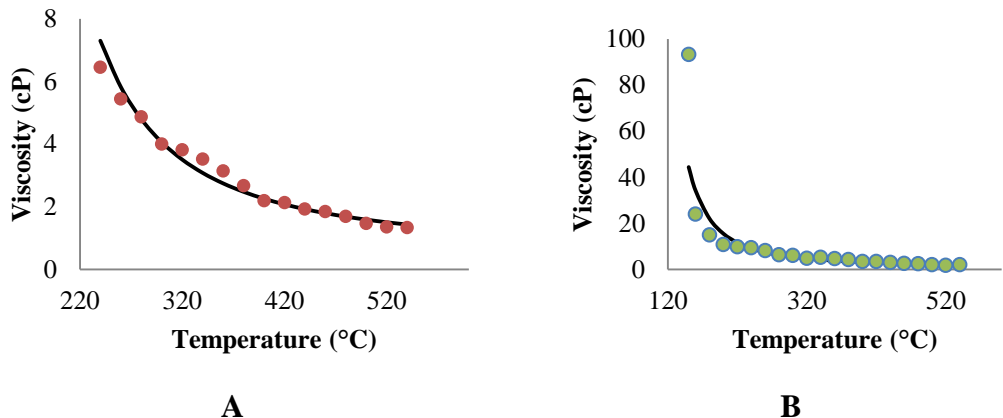


Figure 22: Viscosity (cP) vs. Temperature (°C) from melting temperature up to 550°C for A) LiNa-NO₃ and B) LiK-NO₃ plotted with Arrhenius Fit line.

In the above figure, viscosity (cP) is shown to vary with temperature similarly with the Arrhenius fit line (black) which was constructed using an exponential fit (Figure 22). Activation energies were calculated for both LiNa-NO₃ and LiK-NO₃ and compared

with literature values. Activation energy comparison for the four salts is presented in Table 5 below.

Molten Salt	Calculated Activation Energy (kJ/mol)	Literature Value (kJ/mol)
LiNaK-NO ₃	-	-
NaK-NO ₃	18.4	19.2
LiNa-NO ₃	18.7	-
LiK-NO ₃	21.1	-

Table 5: Activation energies calculated for each molten salt using the Arrhenius model for liquid viscosities as a function of temperature compared to literature values.

7.2: Thermal Conductivity

The process used to calculate thermal conductivity begins by measuring the resistance of the platinum wire while being heated with a current of 3 Amps. This data set, called Resistance(time), is converted to Temperature(time) following the method set forth in section 6.2: Resistance and Temperature Calibration. A sample data set of Resistance(time) is shown below for a 1 mm diameter wire immersed in water at 22°C while being heated with 3 Amps (Figure 23). The thermal conductivity device was confirmed to be accurate by comparing experimental thermal conductivities determined using the aforementioned calibration procedure with known values for two calibration fluids: propylene glycol and distilled H₂O at various temperatures.

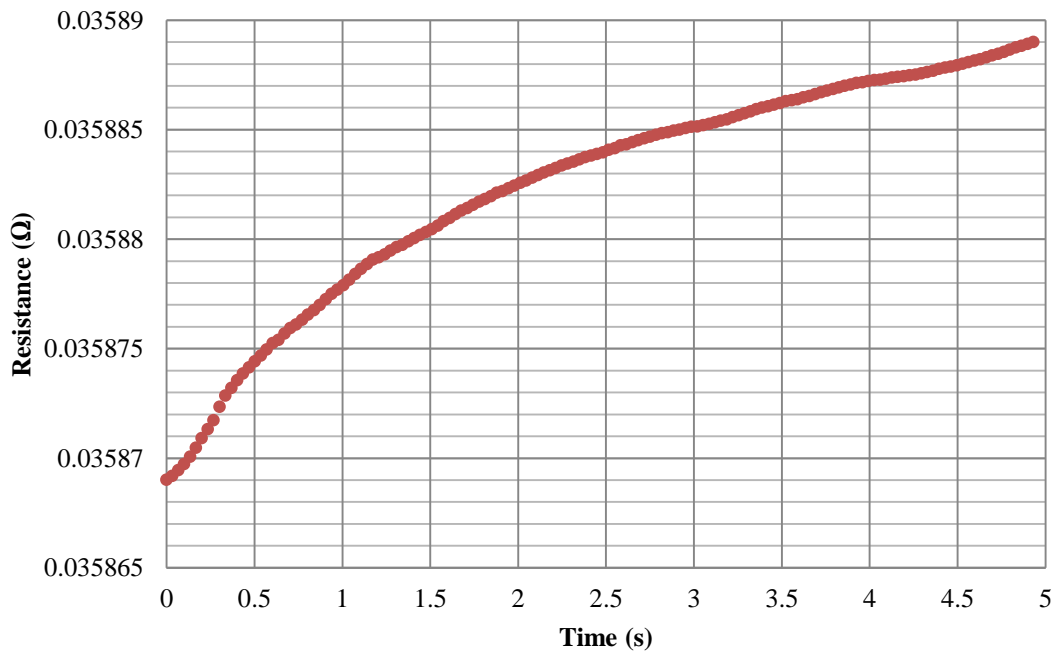


Figure 23: Resistance (Ω) vs. Time (s) for 1 mm diameter platinum wire under 3 Amps of current, immersed in 22°C distilled H₂O.

Temperature(time) data sets are shown below in Figure 24.

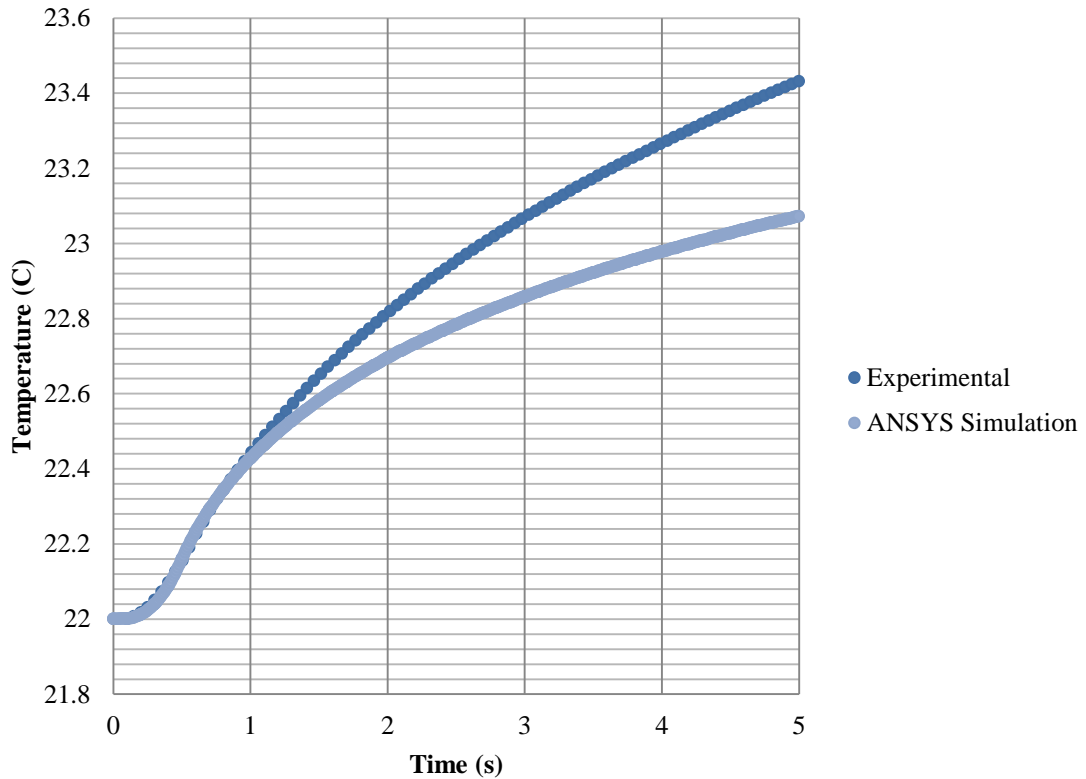


Figure 24: Temperature (°C) vs. Time (s) measured with 3 Amps of current applied to 1 mm platinum wire for 5 seconds immersed in distilled H₂O at 22°C and simulated with ANSYS.

It is clear the temperature profile seen in Figure 24 closely mirrors the resistance profile in Figure 23. By comparing the slopes of this plot in the range ~1-3 seconds to the analytical solution to a thin line heat source put forth in 6.1.1: Analytical Solution for Thin Line Heat Source, thermal conductivity can be calculated via curve fitting. The ANSYS simulation result closely matches the first few seconds of the measurement however due to poor control over the oven temperature, the measured temperature begins to increase past the simulated result after 1.5 seconds.

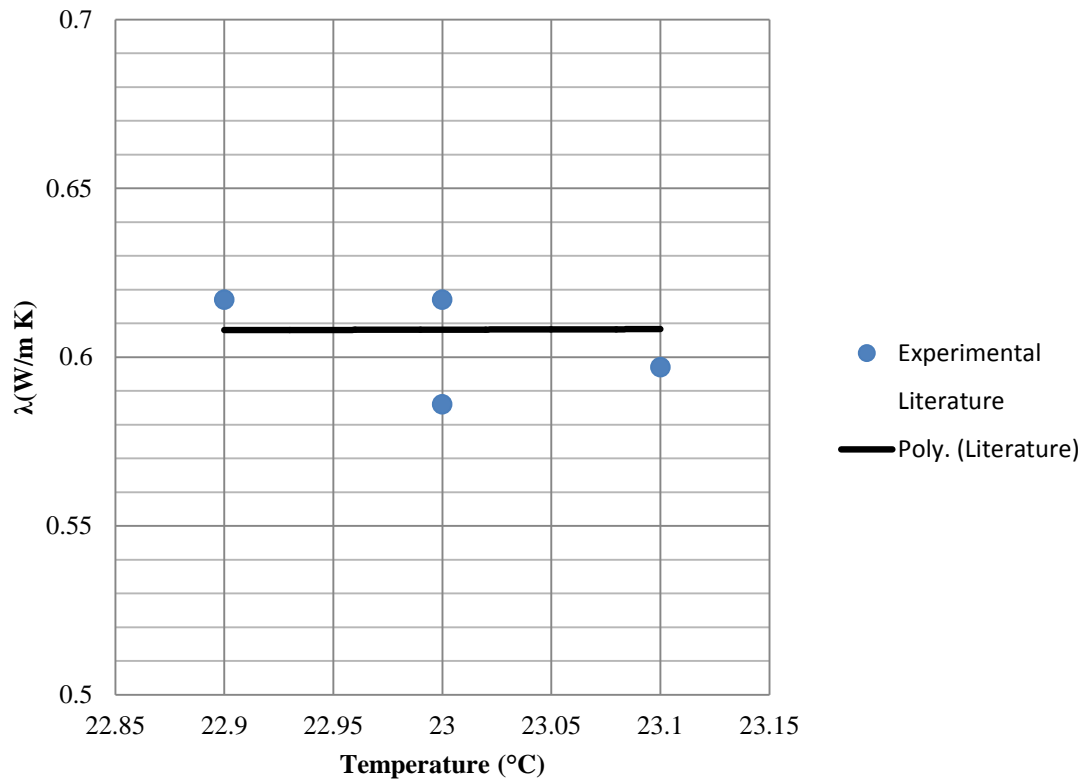


Figure 25: λ (W/m K) vs. Temperature ($^{\circ}$ C) for distilled H₂O near 23 $^{\circ}$ C.

The results showed minimal error between the observed and expected values for the thermal conductivity of water near 23 $^{\circ}$ C (Figure 25). The maximum error between the experimental data and literature values was 3.1%.

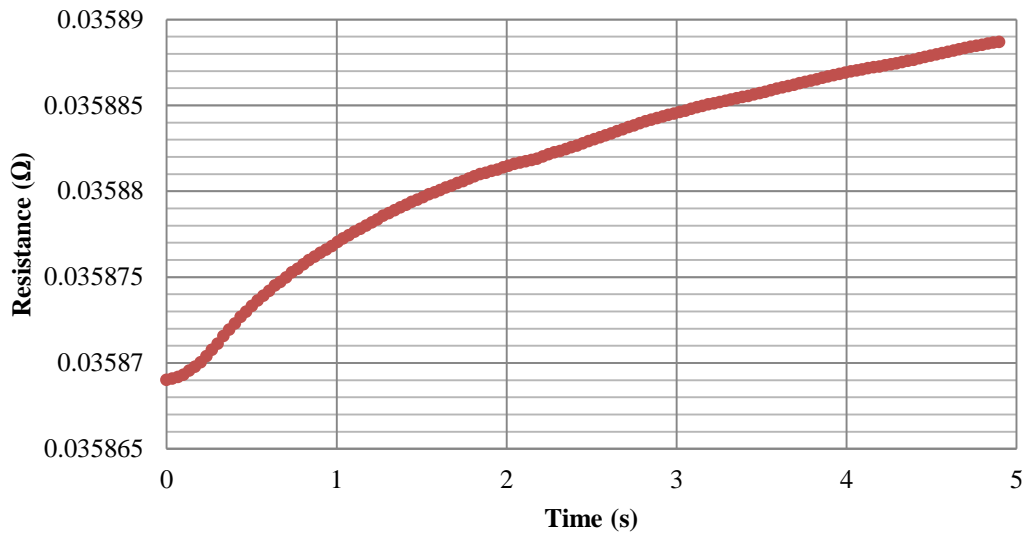


Figure 26: Resistance (Ω) vs. Time (s) for 1 mm diameter platinum wire under 3 Amps of current, immersed in 24°C Propylene Glycol.

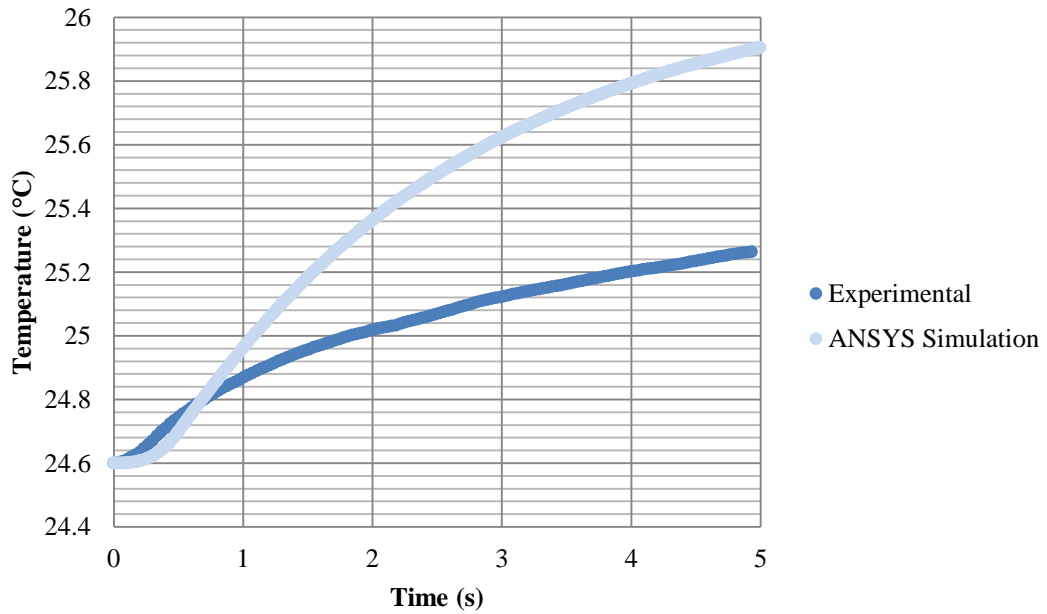


Figure 27: Temperature ($^{\circ}\text{C}$) vs. Time (s) measured with 3 Amps of current applied to 1 mm platinum wire for 5 seconds immersed in Propylene Glycol at 24°C.

It is clear the temperature profile seen in Figure 27 closely mirrors the resistance profile in Figure 26, showing the Resistance(time) and Temperature(time) behavior in the 1 mm wire when immersed in room temperature Propylene Glycol. The ANSYS Simulation is observed to deviate significantly from the experimental data. By comparing the slopes of this plot in the range ~1-3 seconds to the analytical solution to a thin line heat source put forth in 6.1.1: Analytical Solution for Thin Line Heat Source, thermal conductivity was calculated via curve fitting.

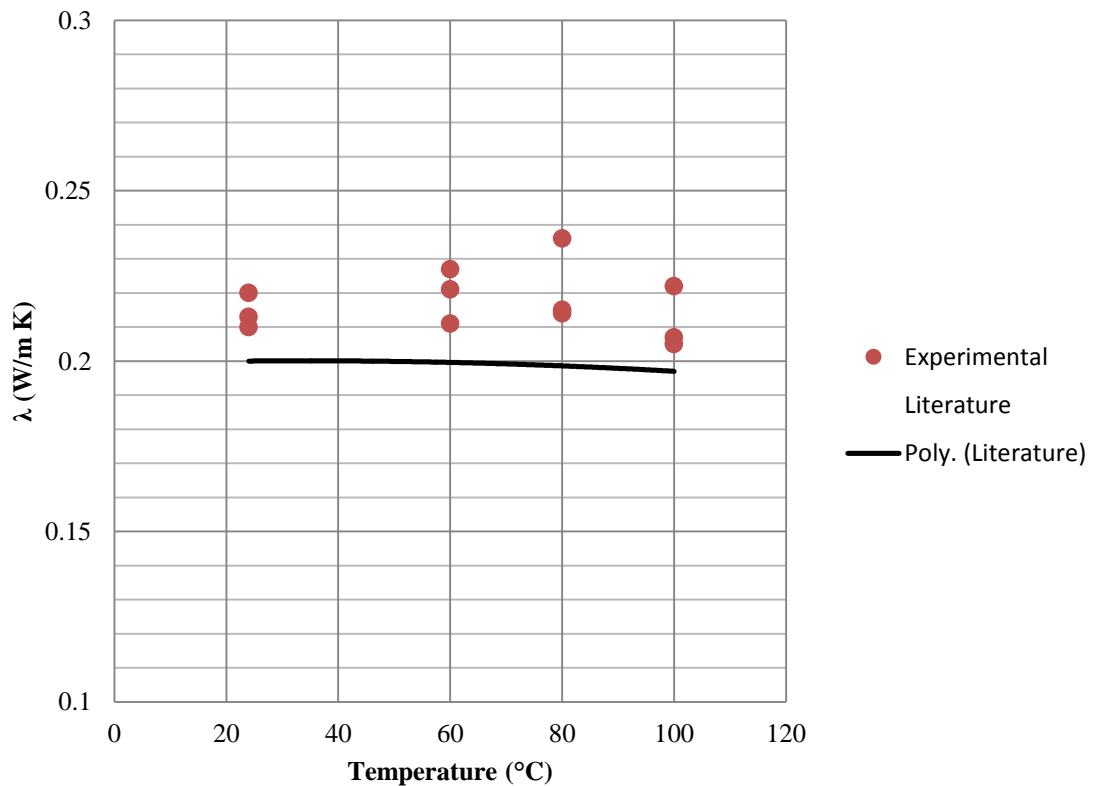


Figure 28: λ (W/m K) vs. Temperature ($^{\circ}$ C) for Propylene Glycol from 24-100 $^{\circ}$ C.

The results showed consistent error between the observed and expected values for the thermal conductivity of propylene glycol over the temperature range 24-100 $^{\circ}$ C

(Figure 28). The maximum error between the experimental data and literature values was 18.9% occurring at a temperature of 80°C.

8: Conclusions

An accurate understanding of the thermo-physical properties of ternary and binary molten salt alkali nitrates are vital to the further development of CSP and thermal energy storage systems. The results contained in the present work have important implications on the design of future solar applications making use of these ternary or binary salts.

The first property analyzed was shear thinning behavior at various temperatures. The results showed that within the intended operating range (130-550°C) these molten salts displayed no shear thinning. Consequently, plant designers can consider a wider range of operating flow rates when optimizing the system.

Next, the viscosity of each molten salt as a function of operating temperature was determined. It is clear at higher temperatures, approaching 550°C, these molten salts to have a viscosity similar to room temperature water (approximately 1.3 cP). The viscosity of LiNaK-NO₃ ternary eutectic salt was observed to be within 8% of the HITEC XL molten salt at 550°C. Some of this difference is accounted by the different chemical structure of the two compounds.

As shown in pressure drop and heat loss simulations contained in the present work, the magnitude of potential heat loss far outweighs the pumping power required to move molten salt at a constant velocity. On the basis of these two variables alone, it appears a lower melting point fluid would be optimal to run a CSP system at night when no power is being generated in order to minimize energy loss. Minimizing heat loss

from the high operating temperatures will be an important design consideration for any efficient CSP system during non-generating hours.

The present work also presents a platinum wire based instrument capable of measuring the thermal conductivity of molten salt nitrates at high temperatures near the upper limit of the operating range. The results from the initial calibration of the thermal conductivity device show low errors when measuring low viscosity fluids like water near room temperature (2%)¹⁸, however significant error was observed compared to the literature values of Propylene Glycol (up to 18%)¹⁸, a more viscous fluid than water. There are several sources of error present. First, limited temperature control in the existing furnace prevents the current test environment from maintaining a constant desired wire temperature. Without precise temperature control, the curve fitting procedure may be fitting experimental data to theoretical data at different temperatures. The error due to temperature control is estimated to be 5% based on observed fluctuations within the furnace. Additionally, the “ramp up” time necessary for the current source to output the desired current is not precisely known, causing a slightly different behavior in the experimental data compared to the theoretical model. The curve fitting method eliminates the majority of this error by analyzing data further removed from the initial (<1 s) ramp up time. The additional sources of error in measuring propylene glycol thermal conductivity are still being refined and reduced. Using this thermal conductivity instrument it is possible to collect crucial thermal conductivity data for the molten alkali nitrate salts presented here.

9: Future Work

Future work required to complete the dataset of thermo-physical properties of molten alkali nitrates salts can be undertaken by verifying the viscosity data presented in this work, and by reducing error in the thermal conductivity instrument. It is suggested that LiK-NO₃ be retested with a working thermocouple to properly determine $\mu(T)$ data.

Due to the experimental setup of the thermal conductivity instrument using an external furnace, precise temperature control is difficult to achieve resulting in constantly fluctuating resistance data leading to error within the calibration procedure. Determining the current ramp up time may be a step towards reducing the error in the instrument. Additionally, further error reduction may be possible by selecting several more calibration liquids with previously determined properties for comparison and adjustment.

References

1. Bauer, T., et al. "Sodium Nitrate for High Temperature Latent Heat Storage." The 11th International Conference on Thermal Energy Storage. June 14-17, 2009. Stockholm, Sweden.
2. Zalba, B., et al. "Review on thermal energy storage with phase change: materials, heat transfer analysis and applications." Applied Thermal Engineering. 23 (2003) 251-283.
3. Lange. Handbook of Chemistry. 1956. Handbook Publisher Inc., Cleveland.
4. Janz, G. J., et al. "Physical Properties Data Compilations Relevant to Energy Storage. II. Molten Salts: Data on Single and Multi-Component Systems." National Standard Reference Data System. (1979) NSRDS-NBS 61, Part II.
5. Nunes, V. M. B., et al. "Viscosity of Molten Sodium Nitrate." International Journal of Thermophysics. 27:6 (2006) 1638-1649.
6. Lança, M., et al. "Viscosity of Molten Potassium Nitrate." High Temperatures – High Pressures. 33:4 (2001) 427-434.
7. Bradshaw, R. "Viscosity of Multi-component Molten Nitrate Salts – Liquidus to 200C." Sandia National Laboratories. March 2010. SAND2010-1129. Livermore, CA.
8. Nagasaka, Y., et al. "The Thermal Conductivity of Molten NaNO₃ and KNO₃." International Journal of Thermophysics. 12:5 (1991) 769-781.
9. Gustafsson, S. E., et al. "Optical Determination of Thermal Conductivity with a Plane Source Technique." Z. Naturforsch. 23a (1968) 44-47.
10. McDonald, J., et al. "Thermal Conductivity of Binary Mixtures of Alkali Nitrates." The Journal of Physical Chemistry. (1969) 725-730.
11. White, L., et al. "Thermal Conductivity of Molten Alkali Nitrates." The Journal of Chemical Physics. 47:12 (1967) 5433-5439.

12. Tufeu, R., et al. "Experimental Determination of the Thermal Conductivity of Molten Pure Salts and Salt Mixtures." International Journal of Thermophysics. 6:4 (1985) 315-330.
13. Santini, R., et al. "Measurement of Thermal Conductivity of Molten Salts in the Range 100-500C." International Journal of Heat and Mass Transfer. 27:4 (1983) 623-626.
14. Bleazard, J., et al. "Thermal Conductivity of Electrically Conducting Liquids by the Transient Hot-Wire Method." Journal of Chemical Engineering Data. 40 (1995) 732-737.
15. Alloush, A., et al. "A Transient Hot-Wire Instrument for Thermal Conductivity Measurements in Electrically Conducting Liquids at Elevated Temperatures." International Journal of Thermophysics. 3:3 (1982) 225-235.
16. Perkins, R. A., et al. "A High Temperature Transient Hot-Wire Thermal Conductivity Apparatus for Fluids." Journal of Research of the National Institute of Standards and Technology. 96:3 (1991) 247-269.
17. Woodfield, P. L., et al. "A Two-Dimensional Analytical Solution for the Transient Short-Hot-Wire Method." International Journal of Thermophysics. 29 (2008) 1278-1298.
18. Rosenzweig, Benjamin. A Calibration Procedure for Measuring the Thermal Conductivity of Molten Salts at Elevated Temperatures. Lehigh University, May 2012.

Vita

Spencer Nelle, the son of Jeffrey and Nancy Nelle was born on September 24, 1988. Raised in Redding, CT, Spencer completed a B.S. degree in Bioengineering at Lehigh University in 2010 and is currently submitting this thesis for completion of the requirements of a Master of Science in Mechanical Engineering.